Heat transfer enhancement of supercritical carbon dioxide in eccentrical helical tubes

Wenguang Li , Zhibin Yu [*]

School of Engineering, University of Glasgow, Glasgow G12 8QQ, UK

ARTICLE INFO

ABSTRACT

A type of eccentrical helical tube (EHT) was proposed for more efficient and compact supercritical carbon dioxide (SCO2) heat exchangers in refrigeration systems. The forced convective heat transfer of SCO2 flowing in three designed eccentrical helical tubes with pitches of 25, 50 mm and eccentricities of 0.9, 1.5 mm was simulated by using the three-dimensional steady Reynolds-averaged Navier-Stokes equations, shear stress transport turbulence model and energy equation in ANSYS CFX 2019 R2 at mass fluxes of 200, 400 kg/m^2s, inlet pressures of 8, 9 MPa, outwards wall heat fluxes of 12, 24 kW/m^2. The flow and heat transfer models were validated in the plain tube with experimental mean heat transfer coefficient and empirical Darcy friction factor. Influences of pitch, eccentricity and operational conditions on heat transfer enhancement were identified. Flow pattern, heat transfer mechanism and vortex kinematics were clarified. Heat transfer enhancement of SCO2 in the EHT was compared with water and air in the EHT, twisted elliptical tube and conical tube, respectively. A pitch of 25 mm and eccentricity of 1.5 mm at 6 mm tube diameter can achieve a better thermal-hydraulic performance. A higher SCO2 mass flux raises Nusselt number and reduces friction factor, a higher inlet pressure and a larger wall heat flux reduces Nusselt number but increases friction factor. The ratio f/f_0 is ranged in 2.52–1.68 and drops off with increasing inlet pressure and nominal Reynolds number, the ratios Nu/Nu_0, ψ and η curves show a concave shape near the pseudocritical point ranged in 1.68–1.06 and 1.06–1.55, 1.23–0.83 and 0.83–1.30, 0.67–0.50 and 0.50–0.92 at the pitch of 25 mm and eccentricity of 1.5 mm, inlet pressure of 8 MPa, mass flux of 400 kg/m^2s, and wall heat flux of 12 kW/m^2. A helical flow pattern with a core flow occurs in the EHT, the local heat transfer coefficient can be correlated to absolute helicity. The high-wall shear stress on the ridge of the EHT is responsible for the heat transfer enhancement. The f/f_0 value of the EHT is in between the twisted elliptical tube and the conical tube, but the Nu/Nu_0 and ψ values are comparable.

1. Introduction

Heat exchangers are critical in carbon dioxide (CO2) refrigeration systems, and their effectiveness in gas side needs to be enhanced [2]. Heat transfer enhancement can be achieved by employing active method, passive method or their combination to generate secondary flows or vortices or intensify turbulence level in boundary layers [3,4]. The active method requires an extra energy to the flow field to accomplish heat transfer enhancement. The passive method, however, does not rely on the extra energy and has simple construction, high reliability, and effortless operation without any moving parts, thus has been applied extensively [3]. Passive methods such as micro-fin-tube [5,6], noncircular tube with multi-lobe cross-section [7], tube with polygon cross-section [8–11], twisted elliptical tube [12], conical tube [13–15],

twisted tape insert [16,17], static mixer [18] and triply periodic minimal surface heat exchanger [19,20] have been proposed and investigated under CO2 cooling flow conditions.

Kuwahara et al. [5] conducted experiments on supercritical carbon dioxide (SCO2) heat transfer with micro-fin tubes under cooling flow conditions at the inlet pressure of 8–10 MPa, mass flux of 360–690 kg/m^2 s and inlet temperature of 20–75 °C. Those tubes had an outlet diameter of 6.02 mm, average inner diameter of 4.76–5.11 mm, fin height of 0.15–0.24 mm, helix angle of 5–25°, number of fins of 46–52 and area expansion ratio of 1.4–2.3. The heat transfer coefficients of the tubes were 1.4–2 times the heat transfer coefficient of the plain tube. Lee et al. [6] performed an experiment on forced convective heat transfer of SCO2 flowing in a micro-fin-tube with an inner diameter of 4.6 mm and outer diameter of 5.0 mm under cooling conditions at 8–10 MPa inlet pressure. The experimental heat transfer coefficient of the micro-fin tube

---

Nomenclature

a_1	constant in μ_t expression of the SST model Eq. (A.11), $a_1=0.31$
c_p	specific heat capacity of fluid at constant pressure, J/kg K
c_{pb}	SCO2 bulk specific heat capacity at constant pressure in the EHT, J/kg K
c_{pb0}	SCO2 bulk specific heat capacity at constant pressure in the plain tube, J/kg K
c_{pw}	SCO2 specific heat capacity at constant pressure at wall in the EHT, J/kg K
c_{pw0}	SCO2 specific heat capacity at constant pressure at wall in the plain tube, J/kg K
d	inner diameter of tube, mm
e	eccentricity of the EHT, as shown in Fig. 1, mm
f	Darcy friction factor of the EHT, defined by Eq. (2)
f_{a0}	Darcy friction factor due to fluid acceleration in the plain tube, defined in Table A2
f_{iso}	Darcy friction factor of the plain tube in isothermal condition
f_0	Darcy friction factor of the plain tube, expressed by Eq. (A.15)
F_1	blending function in the SST k-ω turbulence model
F_2	auxiliary variable in Eq. (A.11) for μ_t
g	acceleration of gravity, $g=9.81$ m/s^2
g_i	specific body force components in Eq. (A.2), m/s^2, $i=1, 2, 3$
G	SCO2 mass flux, kg/m^{2}s
h	SCO2 mean heat transfer coefficient at wall, defined by Eq. (2), W/m^2 K
ℓ	enthalpy of SCO2, J/kg
h_0	SCO2 mean heat transfer coefficient in the plain tube and expressed by Eq. (A.14), W/m^2 K
h_l	SCO2 local heat transfer coefficient in the EHT and defined by Eq. (5), W/m^2 K
H	SCO2 absolute helicity in a tube, defined by Eq. (7), m/s^2
H_b	cross-sectional averaged absolute helicity in a tube, m/s^2
i, j	coordinate index, $i, j=1, 2, 3$
k	turbulent kinetic energy, $k = \frac{1}{2}\overline{u_i'^2}$, m^2/s^2
L	length of the plain tube or EHT, mm
$\dot{m}$	SCO2 mass flow rate, $\dot{m}=\pi G d^2/4$, kg/s
Nu	mean Nusselt number in the EHT, defined by Eq. (3)
Nu_l	local Nusselt number in the EHT, defined by Eq. (5)
Nu_0	mean Nusselt number in the plain tube
p	SCO2 static pressure, Pa
p_1	SCO2 static pressure at the inlet to a tube, MPa
P_{kb}	buoyancy production term in k-equation of the Wilcox k-ω turbulence model Eq. (A.4)
Pr	SCO2 Prandtl number
Pr_b	SCO2 bulk Prandtl number in the EHT, defined by Eq. (8)
Pr_{b0}	SCO2 bulk Prandtl number in the plain tube, defined by Eq. (8)
Pr_t	turbulent Prandtl number, $Pr_t=0.85$
Pr_w	SCO2 Prandtl number at wall in the EHT, calculated by the parameters at wall
Pr_{w0}	SCO2 Prandtl number at wall in the plain tube, calculated by the parameters at wall
$P_{\omega b}$	buoyancy production term in ω-equation of the Wilcox k-ω turbulence model Eq. (A.5)
q_w	wall heat flux of a tube, W/m^2
r	radius of the EHT, mm
Re	nominal Reynolds number of the EHT, $Re = \rho_1 u_1 d /\mu_1$
Re_{b0}	bulk Reynolds number in the plain tube, $Re_{b0}=\rho_{b0}u_{b0}/\mu_{b0}$
Ri	Richardson number, defined by Eq. (9)
s	pitch of the EHT, as shown in Fig. 1, mm

S_E	source term of energy in Eq. (A.3), W/m^3
T	temperature, K
T_1	SCO2 inlet temperature of the EHT, K
T_b	SCO2 bulk temperature in a tube, K
T_{b0}	SCO2 bulk temperature in the plain tube, K
T_f	SCO2 local film temperature, K
T_{f0}	fluid temperature in the plain tube, $T_{f0} = (T_{w0} + T_{b0})/2$, K
T_n	SCO2 temperature at y_n, K
T_w	wall temperature of a tube, K
T_{w0}	wall temperature in the plain tube, K
T^+	dimensionless temperature in the boundary layer expressed in Eq. (A.13)
$\boldsymbol{u}$	SCO2 velocity vector, m/s
u_1	SCO2 velocity at the inlet to the EHT, m/s
u_b	SCO2 bulk velocity in the EHT, m/s
u_{b0}	SCO2 bulk velocity in the plain tube, m/s
u_τ	friction velocity of SCO2 at the nearest wall, m/s
u_i'	turbulent fluctuation velocity components of SCO2, m/s
u_i, u_j	Reynolds time-averaged velocities of SCO2 in coordinate directions i and j, m/s
u_n	SCO2 velocity at y_n, m/s
$u_\tau^{vis}, u_\tau^{log}$	wall friction velocities calculated by using the viscous sub-layer law and logarithmic law, respectively,
x_i, x_j	Cartesian coordinates in directions i and j, m
y_n	distance of a mesh node to the nearest wall, m
y^+	dimensionless wall distance, $y^+ = y_n u_\tau/\nu$
z	axial coordinate of the EHT, m

Greek

α_1, β_1	constants in ω-equation of the Wilcox k-ω turbulence model Eq. (A.5), $\alpha_1=5/9$, $\beta_1=0.075$
α_2, β_2	constants in ω-transformed ε-equation of the standard k-ε turbulence model Eq. (A.7), $\alpha_2=0.44$, $\beta_2=0.0828$
α_3, β_3	blended constants in ω-equation of the SST k-ω turbulence model Eq. (A.8), $\alpha_3=F_1\alpha_1+(1-F_1)\alpha_2$, $\beta_3=F_1\beta_1+(1-F_1)\beta_2$
β	auxiliary variable for T^+ in Eq. (A.13)
β_k	constant in k-equation of the Wilcox k-ω turbulence model Eq. (A.4), $\beta_k=0.09$
β_v	SCO2 thermal expansion coefficient, 1/K
γ	magnitude of the strain rate of SCO2 flow in Eq. (A.11), 1/s
γ_{ij}	strain rate tensor SCO2 flow in Eq. (A.11), 1/s
Γ	auxiliary variable for T^+ in Eq. (A.13)
Δh	mean heat transfer coefficient difference between conservative option and hybrid option, W/m^{2}s
Δp_0	SCO2 static pressure drop across the plain tube, Pa
Δp_{t0}	SCO2 total pressure drop across the plain tube, Pa
ΔT_{ch}	wall temperature difference between conservative option and hybrid option, K
ε	dissipation rate of turbulent kinetic energy, m^2/s^3
ϵ	wall roughness, $\epsilon=0.5$ μm in [1]
η	heat transfer enhancement efficiency, defined by Eq. (1)
λ	thermal conductivity of SCO2, W/m K
λ_b SCO2	bulk thermal conductivity in the EHT, W/m K
λ_{b0}	SCO2 bulk thermal conductivity in the plain tube, W/m K
λ_w SCO2	thermal conductivity at wall in the EHT, W/m K
λ_{w0}	SCO2 thermal conductivity at wall in the plain tube, W/m K
μ	dynamic viscosity of SCO2, Pa.s
μ_1	SCO2 dynamic viscosity at the inlet to the EHT, Pa.s
μ_b	SCO2 bulk dynamic viscosity in the EHT, Pa.s
μ_{b0}	SCO2 bulk dynamic viscosity in the plain tube, Pa.s
μ_t	dynamic viscosity of turbulent eddy, Pa.s
μ_w	SCO2 dynamic viscosity at wall in the EHT, Pa.s
μ_{w0}	SCO2 dynamic viscosity at wall in the plain tube, Pa.s

ν	kinematic viscosity of SCO2, mm^2/s		$\sigma_{\omega 3}$,	blended constant in ω-equation of the SST k-ω turbulence model Eq. (A.8), $\sigma_{\omega 3} = F_1\sigma_{\omega 1} + (1-F_1)\ \sigma_{\omega 2}$
ξ_1, ξ_2	auxiliary variables in Eq. (A10) for blending function F_1		τ_w	area-averaged wall shear stress, Pa
ξ_3	auxiliary variable in Eq. (A.11) for μ_t		τ_{w0}	area-averaged wall shear stress of the plain tube, Pa
ρ	SCO2 density, kg/m^3		ψ	performance evaluation criterion of heat exchanger, defined by Eq. (1)
ρ_1	SCO2 density at the inlet to the EHT, kg/m^3		ω	specific turbulent dissipation rate, 1/s
ρ_b	SCO2 bulk density in the EHT, kg/m^3		ω_n	ω value at y_n, 1/s
ρ_{b0}	SCO2 bulk density in the plain tube, kg/m^3		$\omega_{vis}, \omega_{log}$	ω values calculated by the viscous sub-layer law and logarithmic law, respectively, 1/s
ρ_{cr}	SCO2 density at the pseudocritical point, kg/m^3			
ρ_{f0}	fluid density at the temperature $T_{f0} = (T_{w0} + T_{b0})$ /2, kg/m^3			

Abbreviation

3D	three-dimensional
ρ_w	SCO2 density at wall in the EHT, kg/m^3
CFD	computational fluid dynamics
ρ_{w0}	SCO2 density at wall in the plain tube, kg/m^3
CO2	carbon dioxide
σ_{k1}	constant in k-equation of the Wilcox k-ω turbulence model Eq. (A.4), $\sigma_{k1} = 2$
CT	conical tube
EHT	eccentrical helical tube
σ_{k2}	constant in ω-transformed k-equation of the standard k-ε turbulence model Eq. (A.6), $\sigma_{k2} = 1$
PEC	performance evaluation criterion
RANS	Reynolds-averaged Navier-Stokes
σ_{k3}	blended constant in k-equation of the SST k-ω turbulence model Eq. (A.7), $\sigma_{k3} = F_1\sigma_{k1} + \beta_1(1-F_1)\sigma_{k2}$
SCO2	supercritical carbon dioxide
SST	shear stress transport
$\sigma_{\omega 1}$	constant in ω-equation of the Wilcox k-ω turbulence model Eq. (A.5), $\sigma_{\omega 1} = 2$
TET	twisted elliptical tube
$\sigma_{\omega 2}$	constant in ω-transformed ε-equation of the standard k-ε turbulence model Eq. (A.7), $\sigma_{\omega 2} = 1/0.856$	

was improved by 12–39 % compared with the plain tube.

Li et al. [7] proposed a horizontal noncircular tube with multi-lobe cross-section to improve heat transfer coefficient of SCO2. The multi-lobe cross-section is generated on a circle with multiple inwards arcs. The forced convective heat transfer of SCO2 in 12 tubes with multi-lobe cross-section was simulated by using three-dimensional (3D) steady Reynolds-averaged Navier-Stokes (RANS) equations, shear stress transport(SST) k-ω turbulence model and energy equation at 8.0 MPa inlet pressure, 323.15 K inlet temperature, 0.005652 kg/s mass flow rate and 565.5 W thermal power across tube wall. The heat transfer coefficient of the noncircular tubes was 19–27 % larger than the circular tube, and the friction factor was reduced by 1.7–7.6 %.

Chai and Tassou [8] launched 3D computational fluid dynamics (CFD) simulations of SCO2 flowing in six tubes with circular, semi-circular, square, equilateral triangular, rectangular (aspect ratio=2) and elliptical (aspect ratio=2) cross-sections, respectively. Those tubes had the same hydraulic diameter of 1.22 mm and were subject to cooling and heating conditions. Usually, heat transfer enhancement is evaluated by using friction factor ratio f /f_0, Nusselt number ratio Nu/Nu_0, enhancement efficiency η and performance evaluation criteria (PEC) ψ of a noncircular tube compared with the plain circular tube. The PEC ψ and efficiency η are defined as [21]:

$$\psi = \frac{Nu/Nu_0}{\sqrt[3]{f/f_0}}, \ \eta = \frac{Nu/Nu_0}{f/f_0} \tag{1}$$

where f and Nu are the friction factor and Nusselt number of a noncircular tube, f_0 and Nu_0 are the friction factor and Nusselt number of the circular tube. The plots f/f_0-Re, Nu/Nu_0-Re, and ψ-Re represent the thermal-hydraulic performance of a noncircular tube in heat transfer enhancement compared with the circular tube, where Re is the Reynolds number of the noncircular tube. The ratios f/f_0, Nu/Nu_0, and parameters ψ and η are calculated based on the friction factor and Nusselt number data of the circular, semi-circular, square, triangular, rectangular, elliptical tubes in [8]. The ratio $f/f_0 < 1$ is seen to suggest the hydraulic performance of the semi−circular, square, triangular, rectangular, elliptical tubes is better than the circular tube. However, the ratios $1.04 > Nu/Nu_0 > 1$ and $1.06 > \psi > 1$ and $1.15 > \eta > 1$ occur at Re=20,000–30,000. It implies that heat transfer enhancement caused by these noncircular tubes is very small.

Yang et al. [9] carried out CFD simulations of SCO2 flowing in the horizontal helical coil with non-circular cross sections such as triangle, square, hexagon, octagon, decagon and dodecagon by employing the renormalization group k–ε turbulence model, 3D steady RANS equations and energy equation under cooling conditions. It turned out that the heat transfer coefficient and pressure drop increased with increasing number of edges of polygon. The Nusselt number correlation including curvature for the coil tube with octagon cross-section was obtained but no information about heat transfer enhancement was provided. Pei et al. [10] designed a honeycomb ultra-compact plate heat exchanger with hexagonal channels and predicted numerically the flow and heat transfer characteristics of SCO2 in the hot and cold sides by means of the 3D steady RANS equations, SST k-ω turbulence model and energy equation. The results suggested that ψ=1.23–1.04 in the cold side and ψ=1.20–1.02 in the hot side of the honeycomb ultra-compact plate heat exchanger was obtained compared with the printed circuit heat exchanger at Re=3000–35,000. Wang et al. [11] proposed a novel bio-mimetic honeycomb fractal heat exchanger and simulated the conjugate heat transfer of SCO2 and water in the exchanger. The results indicated that the heat transfer coefficients of SCO2 varied from one channel to another and one location to another. Zhao et al. [12] investigated numerically into the forced convective heat transfer of SCO2 flowing through seven twisted elliptical tubes in a bundle of the shell and tube heat exchanger when the liquid metal at a higher temperature flowed outside the tubes in the counter-flow direction by using the 3D steady RANS equations, standard k-ε turbulence model and energy equation. The heat transfer rate was increased by 68 % and PEC is ψ=1.60 compared with the straight circular tube bundle.

Hashemian et al. [13] simulated the forced convective heat transfer of water through two tube-in-tube heat exchangers with inner conical tube and outer conical or cylindrical tube based on eight cases (each has four cases: two parallel-flow cases and two counter-flow cases) by using the 3D, steady, incompressible RANS equations, standard k-ε turbulence model and energy equation when the cold water (outer tube) inlet temperature was 298 K and hot water (inner tube) inlet temperature was 325 K at Re=12,202–48,808. The numerical results indicated that heat transfer enhancement: f/f_0=2.96–4.56, Nu/Nu_0=1.55–1.48, ψ=1.08–0.89 and η=0.52–0.32 in turbulent flow regime (Re=12,202–48,808) was achieved. This fact suggests that the conical tube is not good at heat transfer enhancement owing to large f/f_0 and small Nu/Nu_0 values in the turbulent flow regime.

Hao et al. [14] simulated the convective heat transfer of SCO2

flowing the conical tube in convergent and divergent flow modes, respectively, based on the 3D RANS equations, SST k-ω turbulence model and energy equation under cooling or heating condition. The heat transfer coefficient in the convergent flow mode was improved by 13.2 % compared with the circular tube under cooling condition but reduced in the divergent flow mode. Yi et al. [15] conducted a numerical study on cooling forced convective heat transfer of SCO2 in the conical microtubes in divergent and convergent flow modes, respectively. It was shown that the heat transfer coefficient was more uniform on the tube wall in the divergent and convergent flow modes than in the circular tube.

Cong et al. [16] simulated the forced convective heat transfer of SCO2 in the circular tube with twisted tape insert using Fluent with modified turbulent Prandtl number under heating condition. The results showed that twisted tape insert could effectively limit heat transfer deterioration and increase turbulence intensity near wall at low flow rate and high wall heat flux, and the smaller twist pitch ratio led to the stronger heat transfer enhancement. Li et al. [17] estimated heat transfer enhancement of SCO2 in the circular tube with a twisted tape insert, ψ=1.18–1.64 was achieved. Meng et al. [18] conducted a simulation of forced convective heat transfer of SCO2 upwards flowing in a straight circular tube with a static mixer having three helical blades by using the 3D steady RANS equations, SST k-ω turbulence model and energy equation at the Reynolds numbers of 7900–22,385 under heating conditions, and it turned out that the buoyancy effect was eliminated by 99.83-99.97% by the mixer. Li et al. [19] and Li et al. [20] investigated heat transfer enhancement of SCO2 in the triply periodic minimal surface heat exchanger.

Recently, the eccentrical helical tube (EHT) has been explored to enhance heat transfer inside or outside the tube [22–26]. The EHT was proposed for water in [22] firstly, then was applied to the tube bundle of a shell and tube heat exchanger in [23]. Very recently, the EHT was combined with one helical tape attached to the wall [24] for air, and integrated to a tube-in-tube heat exchanger for water in [25] and for Al$_2$O$_3$/water nanofluid [26], respectively. Ma et al. [22] designed an EHT with length=480 mm, inner diameter=20 mm, eccentricity e=3 mm (eccentricity ratio=3/20) and pitch s=120 mm, and the forced convective heat transfer of water flowing in the EHT was predicted using the 3D, steady, incompressible Navier-Stokes equations and energy equation in laminar flow regime (Re=300–1800) in Fluent at a uniform temperature of 350 K. The best heat transfer enhancement: f/f_0=2.14, Nu/Nu_0=2.81, ψ=2.18 and η=1.32 was achieved at Re=1800. Yang et al. [23] designed a shell and tube heat exchanger with EHTs for oil cooler and predicted the thermal-hydraulic performance of the tube side (hot oil) and shell side (cold water) separately in Fluent 6.3 at constant wall temperatures. The forced convective heat transfer of the hot oil was in laminar flow regime (Re=300–1800), but the heat transfer of the cold water was in turbulent flow regime (Re=5000–14,000). The heat transfer enhancement inside the EHT was predicted as f/f_0=1.45–2.78, Nu/Nu_0=1.46–2.89, ψ=1.29–2.06, and η=1.01–1.04 compared with the plain tube at Re=300–1800. Alsulaiei et al. [24] evaluated the thermal-hydraulic performance of air in an EHT (length=1000 mm, inner diameter=20 mm) with a twisted full-length tape attached to the inner wall based on the 3D, steady, incompressible RANS equations, SST k-ω turbulence model and energy equation in turbulent flow regime (Re=4000–10,000) with ANSYS Fluent 17.0 under heating condition (constant wall flux of 1.7 kW/m^2). The results showed that a larger tape height led to a higher Nusselt number but a greater friction factor. The best PEC, i.e., ψ=2.07 at Re=4000 and ψ=1.69 at Re=10,000 was obtained at the height ratio of 0.625. Razzaq et al. [25] designed three tube-in-tube heat exchangers (length=1 m) with inner EHT (diameter=25 mm, pitch ratio=5, 10, and 15) and outer cylindrical tube (diameter=50 mm). The forced convective heat transfer in these exchangers was simulated by using ANSYS Fluent 18.2 based on the 3D, steady, incompressible RANS equations, standard k-ε turbulence model and energy equation in turbulent flow regime when the inlet

temperature of the hot water in the inner tube and the cold air in the outer tube was 343 K and 298 K at Re=5000–30,000. The heat exchanger effectiveness was calculated. It was showed that the best overall thermal-hydraulic performance was achieved at the pitch ratio of 5, resulting the effectiveness increased by 14.8 %. Razzaq et al. [26] simulated the effect of Al$_2$O$_3$/water nanofluid on the thermal-hydraulic performance of the tube-in-tube heat exchanger with the inner EHT at the pitch ratio of 5 in [25] at Re=5000–30,000. The numerical methods and flow models were identical to those in [25] but the nanoparticle volume fraction-dependent effective thermophysical and transport properties were employed for the nanofluid. The nanoparticle volume fractions were 0.05, 1, 2.5, and 4 %. The results demonstrated that the effectiveness of the heat exchanger was improved by 6 % at the volume fraction of 4 % compared with the water flow condition. The pressure drop rose with increasing nanoparticle volume fraction.

Based on the existing two sets of CFD simulation results, the heat transfer enhancement: f/f_0=1.25–2.14, Nu/Nu_0=1.23–2.81, ψ=1.14–2.18 and η=0.98–1.32 [22] or f/f_0=1.45–2.78, Nu/Nu_0=1.46–2.89, ψ=1.29–2.06, and η=1.01–1.04 [23] in laminar flow regime (Re=300–1800) was obtained, and the enhancement: f/f_0=2.80–2.21, Nu/Nu_0=2.78–2.03, ψ=2.07–1.56 and η=0.88–0.84 in turbulent flow regime (Re=4000–10,000) was indicated [24]. This fact suggests that the EHT has a better performance in heat transfer enhancement, i.e., lower f/f_0, higher Nu/Nu_0, ψ and η than the conical tube in turbulent flow regime.

Two eccentrical helical tubes were designed and the forced convective heat transfer of SCO2 flowing in them was simulated by adopting the 3D RANS equations, SST k-ω turbulence model and energy equation at a constant wall flux in cooling conditions in the article. The heat transfer enhancement of SCO2 was determined by comparing the thermal-hydraulic performance with that of SCO2 through the plain tube at the same nominal Reynolds number. The effects of pitch ratio, SCO2 mass flux, inlet pressure and wall heat flux were clarified. The novelty of the article relies on: (1) the first trial on heat transfer enhancement of SCO2 in EHTs; (2) heat transfer enhancement across the pseudocritical point; (3) heat transfer enhancement explained by wall shear stress and vortex kinematics.

2. Design, models and validation

2.1. EHT design

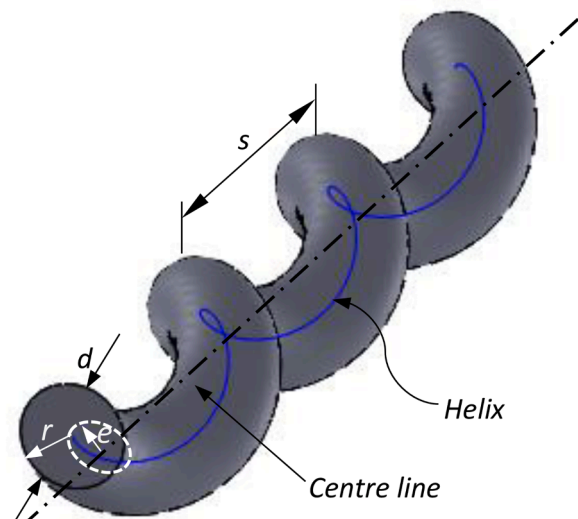Essentially, an EHT is a helical coil with a helix as its baseline and the

Fig. 1. Eccentrical helical tube with dimensions such as tube radius r, helix eccentricity e and pitch s.

constrain $r>e$, see Fig. 1, where e, d, r and s are the eccentricity, diameter, radius and pitch of the helix, respectively. When the condition $r \ll e$ is valid, however, the EHT becomes a helical coil. Particularly, when e approaches zero, an EHT becomes a straight circular tube. Note that the pitch is defined as the propagating axial distance when the helix turns around the center line by a 360° circumferential angle. The pitch ratio s/d and eccentricity ratio e/d are the important dimensionless parameters for EHTs.

The experimental counter-flow tube-in-tube heat exchanger in [27] was employed as the reference heat exchanger. The original inner circular tube of the exchanger was replaced with a newly designed EHT whose inner diameter of 6 mm and length of 500 mm are the same as those of the original tube. The pitch s and eccentricity e or pitch ratio s/d and eccentricity ratio e/d are two design variables for a new EHT. The existing pitch s and eccentricity e or pitch ratio s/d and eccentricity ratio e/d are listed in Table 1. In the paper, the pitch s=25, 50 mm and eccentricity e=0.9, 1.5 mm are selected to investigate their effects on the heat transfer enhancement inside the EHT. As a result, the pitch ratio s/d and eccentricity ratio e/d are in the range shown in the literature.

2.2. Models

EHT geometrical models were generated in Solidworks and then read into ANSYS DesignModeler to create a fluid domain. First, a helix is specified with a known eccentricity and pitch and number of revolutions as well as start angle. Second, an initial cross-section of the EHT is defined at the start point of the helix, then the cross-section is swept along the helix to generate the EHT model. Finally, 15d long extension plain tubes are extruded from the inlet and outlet of the EHT each upstream and downstream to guarantee a fully developed flow in the EHT. A generated EHT geometrical model for CFD simulations is illustrated in Fig. 2.

The counter-flow tube-in-tube heat exchanger with the plain tubes in [27] was employed as the reference heat exchanger, the length (500 mm) and diameter (d=6 mm) of the EHT length are equal to those of the inner tube of the reference heat exchanger. The cooling effect of the outer tube in the reference heat exchanger is replaced with a known uniform outwards wall heat flux q_w. Walls of the upstream and downstream extension tubes are adiabatic.

The CFD software ANSYS CFX 2019 R2 was selected to perform the forced convective heat transfer of SCO2 flowing in the EHT by using 3D, steady, subsonic, compressible SCO2, RANS equations, energy equation and SST k-ω turbulence model along with a blended wall function-Automatic Near-Wall Treatment. Their corresponding equations are listed in Appendix A.

The cases studied for heat transfer enhancement by using EHTs in the paper are tabulated in Table 2. There are nine cases for EHTs to investigate into the effects of pitch, eccentricity, SCO2 mass flux, inlet pressure, and wall heat flux on heat transfer enhancement. For the plain tube, there are four cases to provide the reference f_0 and Nu_0 for

evaluating heat transfer enhancement.

Both temperature- and pressure-dependent SCO2 thermophysical and transport property constants were determined by using the REFPROP Version 9.0 program [28]. Based on them a real gas property table file was generated and read into CFX-Pre to interpolate these constants with local temperature and pressure in the fluid domain. The high-resolution scheme was specified to the advection terms in Eqs. (A.2)-(A.5), respectively. The root-mean-square tolerance residual errors of the variables in those equations were prescribed to be 10^{-4}.

A known SCO2 inlet pressure p_1 and inlet temperature T_1, zero velocity gradient and 5 % turbulence intensity are provided for the EHT inlet, and a SCO2 mass flow rate $\dot{m}$ is prescribed at the EHT outlet, where $\dot{m}=\pi G d^2/4$. A known uniform outwards wall heat flux q_w is assigned to the EHT wall, a zero-wall heat flux (adiabatic) is imposed on the walls of two extension tubes. All the walls are smooth, and no slip condition is implemented on them.

2.3. Validation

The counter-flow tube-in-tube heat exchanger in [27] was employed to validate the flow and heat transfer models and numerical methods above. Like [29], the heat exchanger is simplified to a sole tube model shown in Fig. A1(a), and the annulus between the inner tube and the outer tube is removed, the water-cooling effect on the hot SCO2 is realised by using a known experimental uniform outwards wall heat flux q_w. The experimental mean heat transfer coefficient h of the inner tube at various SCO2 inlet temperature was extracted from [27] and are compared with that predicted by CFD simulation. The mean error of the heat transfer coefficient between simulation and experiment is -5.7 ± 8.8 %, suggesting the heat transfer coefficient being underestimated by 5.7 % on average. More information about the validation is presented in Appendix A.

2.4. Mesh size independence

Four sets of wedge element dominant mesh with an inflation layer near the walls, i.e. Mesh 1 to Mesh 4, were generated in the fluid domain of the EHT with s=25 mm and e=1.5 mm, the information on them and the corresponding y^+ values determined under conditions of T_1=26–65 °C, p_1=8 MPa, G=400 kg/m²s, q_w=12 kW/m² are listed in Table 3. The mean heat transfer coefficient h and friction factor f are plotted against number of elements of Mesh1 to Mesh 4 are illustrated in Fig. 3.

The SCO2 mean heat transfer coefficient h and Darcy friction factor f are calculated by using the following equations:

$$h = \frac{q_w}{T_b - T_w}, \quad f \approx \frac{8\tau_w}{\rho_b u_b^2} \tag{2}$$

where T_b is SCO2 bulk temperature in the EHT, which is the arithmetic mean of 12 area-averaged SCO2 temperatures in ten cross-sections uniformly distributed as [27] in the EHT and inlet and outlet to the EHT; T_w is area-averaged wall shear stress, q_w is the given wall heat flux, u_b and ρ_b are SCO2 bulk velocity and density in the EHT, and calculated by using the same algorithm as T_b, τ_w is area-averaged wall shear stress. The formula for f is found in [30]. Since the Darcy friction factor f calculated by using the mean wall shear stress is closer to the friction factors predicted with two popular empirical formulas for the plain tube in Appendix A, the friction factor f based on the area-averaged wall shear stress is adopted.

Based on Fig. 3(a) it is seen that h shows little variation from Mesh 2 to Mesh 3, indicating the mesh size independence achieved at T_1=65 °C. However, f still varies with number of mesh elements. In Fig. 3(b), it is shown that the mesh size independence is achieved at Mesh 3 and Mesh 4 for h as T_1 varies in 26–65 °C. The mesh size independence arrives at T_1=26–34.5 °C (y^+=1.16–1.86), but f still depends on mesh size at T_1=35–65 °C (y^+=2.07–3.15). This suggests that a denser mesh is

Table 1
Comparison of geometrical parameters of EHTs between present designs and those in the literature.

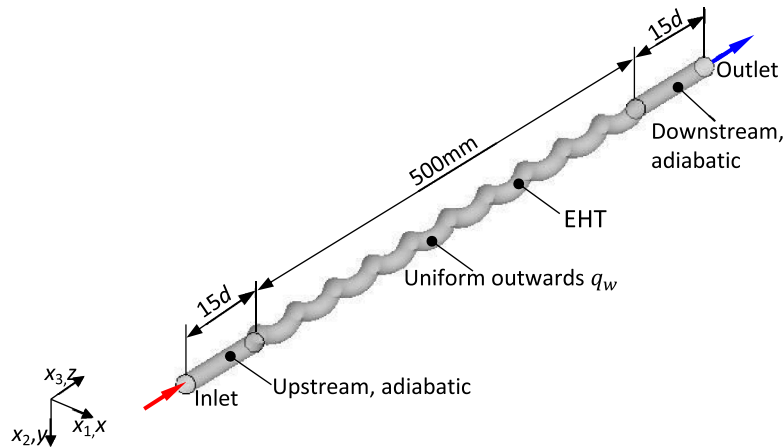| Refs.	d(mm)	e(mm)	s(mm)	e/d	s/d
[22](Ma,2012)	20	3	120	0.15	6
[23](Yang,2014)	14	2.5	40	0.18	2.86
[24](Alsulaiei,2021)	20	5	60	0.25	3
	20	5	100	0.25	5
[25](Razzaq,2021)	25	6.5	290	0.26	11.6
	25	6.5	580	0.26	23.2
	25	6.5	870	0.26	34.8
[26](Razzaq,2022)	25	6.5	290	0.26	11.6
Present	6	0.9	25	0.15	4.17
	6	1.5	25	0.25	4.17
	6	1.5	50	0.25	8.33

Fig. 2. EHT geometrical model generated for CFD simulations, d is the inner diameter of the EHT, d=6 mm, the tube-in-tube heat exchanger with two plain tubes in [27] is selected as the reference heat exchanger in the paper, the EHT and the inner tube of the reference heat exchanger share the same diameter (6 mm) and length (500 m).

Table 2
Cases studied for heat transfer enhancement of SCO2 by using EHTs.

Case	Plain tube			Case	EHTs				
	p_1 (MPa)	G (kg/m^2 s)	q_w (kW/m^2)		p_1 (MPa)	G (kg/m^2 s)	q_w (kW/m^2)	s (mm)	e (mm)
1	8	200	12	1	8	200	12	25, 50	1.5
2	8	400	12	2	8	400	12	25, 50	1.5
3	9	400	12	3	9	400	12	25, 50	1.5
4	8	400	24	4	8	400	24	25, 50	1.5
total	4			5	8	400	12	25	0.9
Note that T_1=25–70 °C in each case for plain tube and EHTs.				total	$4 \times 2 + 1 = 9$				

Table 3
Information on four sets of mesh used in CFD simulations of forced convective heat transfer of SCO2 in the EHT with s=25 mm and e=1.5 mm.

Item		Mesh 1	Mesh 2	Mesh 3	Mesh 4
Element size(mm)		0.375	0.375	0.35	0.33
Nodes		1743,679	1964,636	2090,760	2376,694
Elements	Total	4155,456	4681,777	5123,134	5875,304
	Tet4	1160,586(27.9 %)	1287,591(27.5 %)	1598,254(31.2 %)	1892,024(32.2 %)
	Wed6	2994,870(72.1 %)	3394,186(72.5 %)	3524,880(68.8 %)	3983,820(67.8 %)
Element quality		0.3103±0.3320	0.2804±0.3460	0.3081±0.3584	0.3097±0.3647
Aspect ratio		23.35±24.53	41.99±48.24	34.39±38.01	38.60±43.35
Skewness		0.1799±0.1139	0.1745±0.1105	0.1821±0.1149	0.1903±0.1181
Orthogonal quality		0.8194±0.1134	0.8247±0.1099	0.8168±0.1141	0.8086±0.1172
Inflation boundary layer	First layer height(mm)	0.005	0.0025	0.003	0.0025
	Number of layers	15	17	15	17
	Growth rate	1.2	1.2	1.2	1.2
	y^+(p_1=8 MPa, T_1=26–65 °C, G=400 kg/m^{2}s, q_w=12 kW/ m^2)	2.34–6.19	1.16–3.15	1.39–3.72	1.12–3.10

where Tet4–4-node tetrahedral element, Wed6–6-node wedge element, d–inner diameter of the tube, mm, G–mass flux of SCO2, kg/m2s, y^+–dimensionless wall distance, $y^+ = y_n u_\tau / \nu$, y_n–distance of a mesh node to the nearest wall, u_τ – friction velocity of SCO2 at the nearest wall, ν–kinematic viscosity of SCO2

required on the right of the pseudocritical point than on the left due to the decreasing dynamic viscosity of SCO2. Because of the limitation in computing resources even more dense meshes are not attempted, and Mesh 3 is kept in use in the paper.

3. Results

The results of CFD simulations on the forced convective heat transfer of SCO2 in various EHTs are presented in terms of thermal-hydraulic performance, heat transfer enhancement, and heat and fluid flow. The thermal-hydraulic performance of the EHTs is characterised by employing mean Nusselt number Nu and Darcy friction factor f. The mean Nusselt number is defined by using SCO2 mean heat transfer co-efficient h, bulk thermal coducivity λ_b and EHT diameter d as:

$$Nu = \frac{hd}{\lambda_b} \quad (3)$$

where λ_b is the arithmetic mean of 12 area-averaged SCO2 thermal conductivities in ten cross-sections uniformly distributed in the EHT and inlet and outlet to the EHT. The formulas for h and f have been expressed by Eq. (2).

The heat transfer enhancement is evaluated by means of four parameters: f/f_0, Nu/Nu_0, ψ and η, here f_0 is devoted to the Darcy friction factor of the plain tube and defined by the first expression in Eq. (A.15) in Appendix A, Nu_0 is SCO2 mean Nusselt number in the plain tube, and defined as:
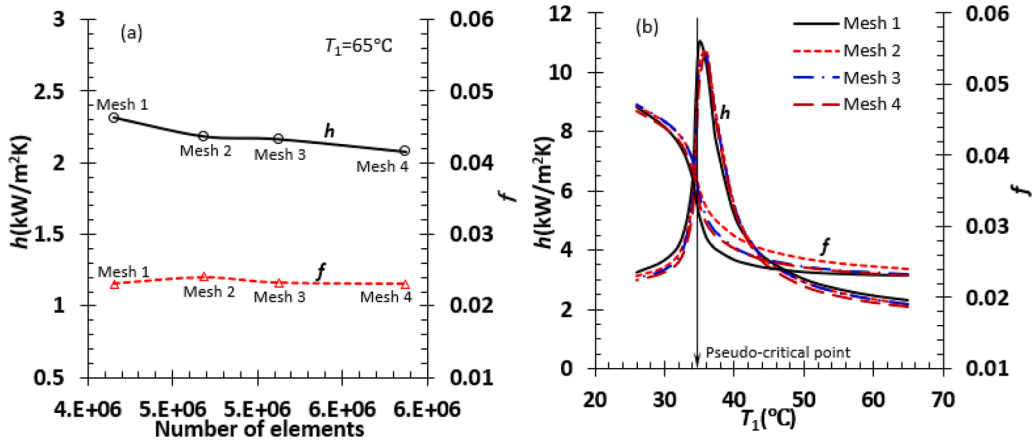
Fig. 3. Mean heat transfer coefficient h and Darcy friction factor f are plotted against number of elements of Mesh 1 to Mesh 4 at inlet temperature T_1=65 °C (a), mean heat transfer coefficient h and friction factor f are plotted against inlet temperature T_1 at Mesh 1 to Mesh 4 (b) for the EHT with s=25 mm and e=1.5 mm under the conditions of p_1=8 MPa, G=400 kg/m²s, q_w=12 kW/m².

$$Nu_0 = \frac{h_0 d}{\lambda_{b0}} \tag{4}$$

where λ_{b0} is SCO2 bulk thermal conductivity, and obtained from CFD simulation results in the plain tube, h_0 is calculated by Eq. (A.14) in Appendix A.

Heat and fluid flow is associated with SCO2 temperature and velocity

or other variable distributions in the EHTs and can provide an insight into mechanisms for heat transfer enhancement.

3.1. Thermal-hydraulic performance

Thermal-hydraulic performance of EHTs is affected by EHT geometrical parameters, and SCO2 operational conditions. Here the EHT
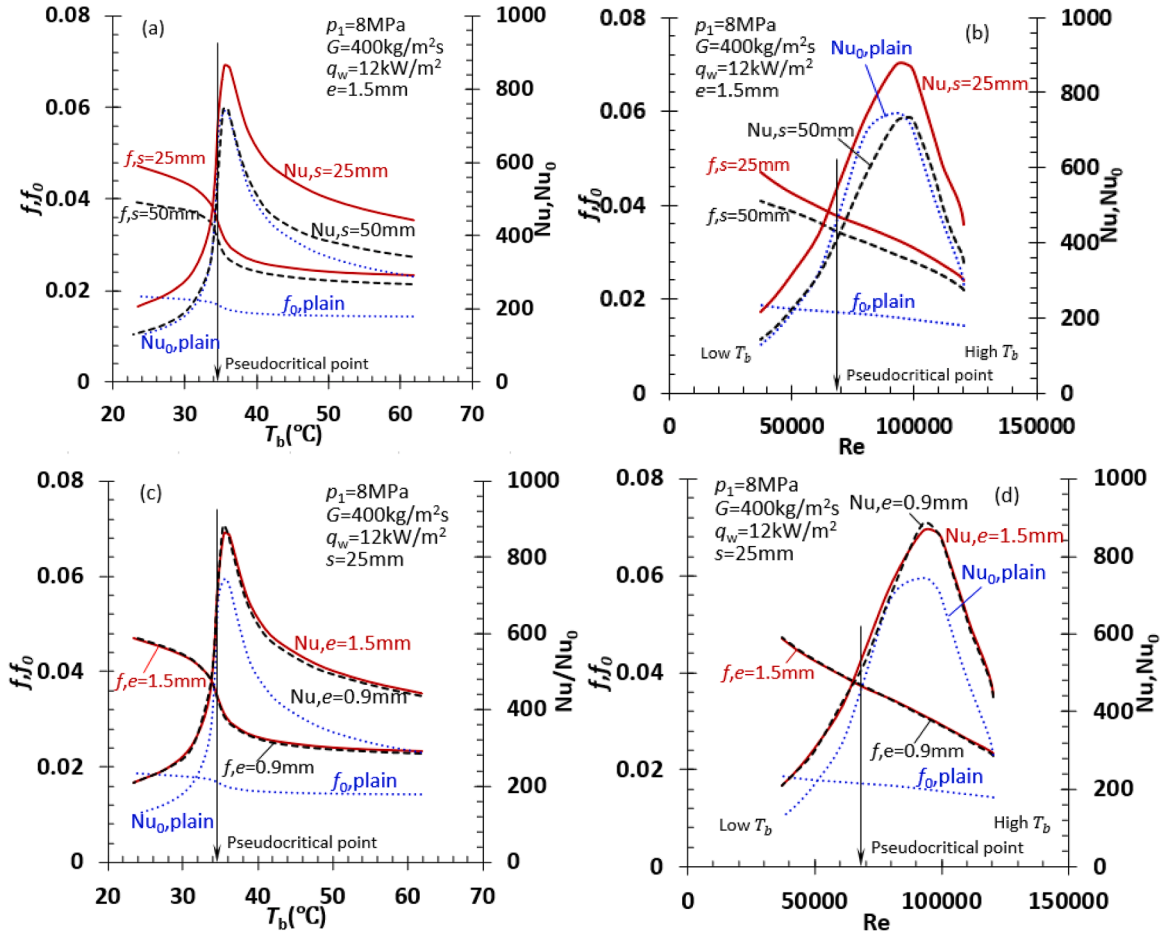
Fig. 4. Mean Nusselt number Nu and Darcy friction factor f of two EHTs, mean Nusselt number Nu_0 and Darcy friction factor f_0 of the plain tube are plotted against bulk temperature T_b and nominal Reynolds number Re, (a) and (b) for the EHTs with s=25, 50 mm at e=1.5 mm, (c) and (d) for the EHTs with e=0.9, 1.5 mm at s=25 mm.

geometrical parameters mainly indicate pitch and eccentricity, the operational conditions include SCO2 mass flux and inlet pressure and wall heat flux.

3.1.1. Effect of pitch and eccentricity

Effects of pitch and eccentricity are investigated under the operational conditions of p_1=8 MPa, G=400 kg/m²s, q_w=12 kW/m² by altering s=25, 50 mm at $e = 1.5$ mm, and $e = 0.9$, 1.5 mm at s=25 mm, respectively. The corresponding mean heat transfer coefficients and Darcy friction factors of the EHTs are illustrated in Fig. 4 against SCO2 bulk temperature T_b and nominal Reynolds number Re. The mean heat transfer coefficients and Darcy friction factors of the plain tube under the same operational conditions are included in the figure for comparison. The nominal Reynolds number Re is based on the inlet flow conditions, $Re = \rho_1 u_1 d/\mu_1$, where u_1, ρ_1 and μ_1 are SCO2 velocity, density and dynamic viscosity at the inlet to an EHT.

It is seen that the curves of f and f_0 versus T_b and Re are similar in shape. With increasing s, the f curves of the EHTs shift upwards, and are higher than the f_0 curve. This suggests that the Darcy friction factor f rises with increasing s at a given T_b or Re. The curves of Nu and Nu_0 versus T_b and Re are similar in shape, but also the Nu curves of the EHTs move downwards with increasing s and are above the Nu_0 curve. This means that heat trasnfer enhancement occurs in the EHTs and is subject to a certain more pressure drop penalty in comparison with the palin tube.

When the eccentricity e is increased to 1.5 mm from 0.9 mm, the f and Nu curves of the EHTs remain unmoved basically. In this regard, the eccentricity has a negiiliable effect on the thermal-hydarulic performance of the EHTs in the paper.

3.1.2. Effect of mass flux

The effect of SCO2 mass flux on the thermal-hydraulic performance is identified under the conditions of p_1=8 MPa, q_w=12 kW/m², s=25 mm, and e=1.5 mm by employing G=200, 400 kg/m²s, respectively. The mean heat transfer coefficients and Darcy friction factors of the EHT and plain tube are shown in Fig. 5 against T_b and Re. It is observed that an increasing SCO2 mass flux raises Nusselt numbers Nu and Nu_0 but reduces friction factors f and f_0 significantly. This is because a decreased G means a lowed Re, subsequently an enlarged friction factor at a given d.

3.1.3. Effect of inlet pressure

The effect of SCO2 inlet pressure is clarified by using p_1=8, 9 MPa under the conditions of G=400 kg/m²s, q_w=12 kW/m², s=25 mm and e=1.5 mm. The corresponding f and Nu curves of the EHT are shown in Fig. 6 along with the f_0 and Nu_0 curves of the plain tube for comparison. The inlet pressure is observed to influence Nu and Nu_0 more significantly than f and f_0. With increasing p_1, the SCO2 pseudocritical points move to a higher temperature and the Nu and Nu_0 peaks get smaller, and the Nu and Nu_0 curves become flattened. For the plain tube, the effect of inlet pressure on the f_0 curve is marginal.

3.1.4. Effect of wall heat flux

The influence of imposed wall heat flux is studied by making use of q_w=12, 24 kW/m² under the conditions of G=400 kg/m²s, p_1=8 MPa, s=25 mm and e=1.5 mm. The predicted f and Nu curves of the EHT as well as f_0 and Nu_0 curves of the plain tube are demonstrated in Fig. 7. The wall heat flux is shown to affect Nu and Nu_0 more considerably than f and f_0; particularly, the larger the wall heat flux, the higher the Nu and Nu_0, and the greater the f and f_0.

3.2. Heat transfer enhancement

Heat transfer enhancement in the thermal-hydraulic performance of SCO2 in the EHTs is evaluated by comparing f and Nu of the EHT with the counterpart of the plain tube. As a result, four parameters: f/f_0, Nu/Nu_0, ψ and η, where ψ and η are defined by Eq. (1), exist and are employed for that purpose. Effects of geometrical parameters of the EHT and SCO2 operational conditions on the heat transfer enhancement are described in next two sections.

3.2.1. Effect of geometrical parameters

The curves of four heat transfer enhancement parameters: f/f_0, Nu/Nu_0, ψ and η are shown against T_1 and Re in Fig. 8 under the conditions of G=400 kg/m²s, p_1=8 MPa, q_w=12 kW/m² and e=1.5 mm when s=25 mm and 50 mm are held, respectively. It turns out that f/f_0 decreases with increasing T_1 and Re but is ranged in 2.52–1.68 at s=25 mm, and 2.19–1.53 at s=50 mm. Nu/Nu_0 decreases towards the pseudocritical point and is in the ranges of 1.68–1.06 and 1.06–1.55 at s=25 mm, 1.12–0.83 and 0.83–1.20 at s=50 mm, respectively. The shape of ψ and η curves is similar to the shape of Nu/Nu_0 curves at s=25, 50 mm. ψ varies with increasing T_1 and Re in the ranges of 1.23–0.83 and 0.83–1.30 at s=25 mm, 0.86–0.67 and 0.67–1.04 at s=50 mm, respectively. η is ranged in 0.67–0.50 and 0.50–0.92 at s=25 mm, and 0.51–0.44 and 0.44–0.79 at s=5omm, respectively. Basically, $\psi \leq 1$ is held in the entire range of T_1 and Re at s=50 mm.

Based on the ψ and η values, the pitch s=25 mm is the most suitable choice for a better heat transfer enhancement of SCO2 flowing in the EHT. Since $\psi<1$ occurs in the region near the pseudocritical point, the heat transfer enhancement is less effective in that region.
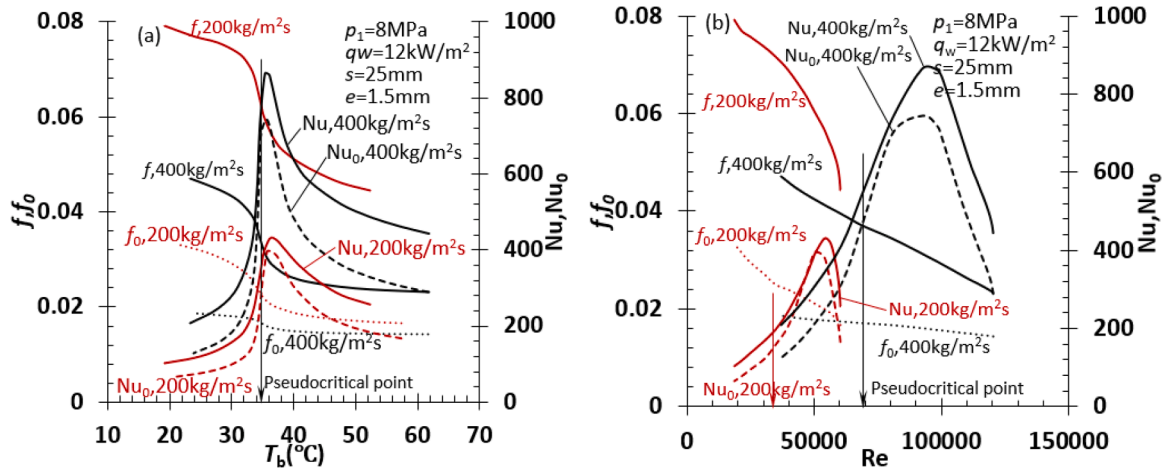

Fig. 5. Mean Nusselt number *Nu* and Darcy friction factors *f* of the EHT with *s*=25 mm and *e*=1.5 mm, mean Nusselt number *Nu*₀ and Darcy friction factor *f*₀ of the plain tube are plotted against bulk temperature T_b (a) and nominal Reynolds number Re (b) at G=200, 400 kg/m²s.
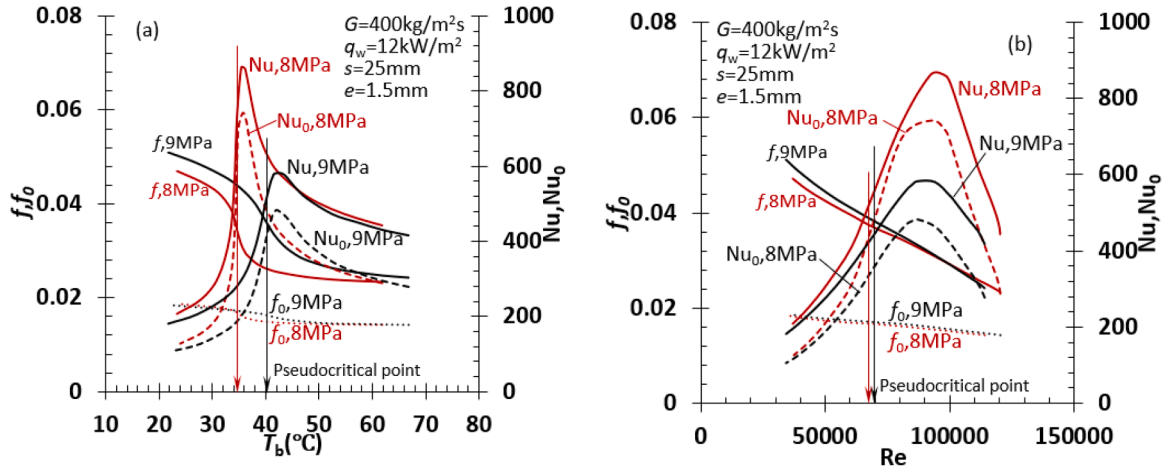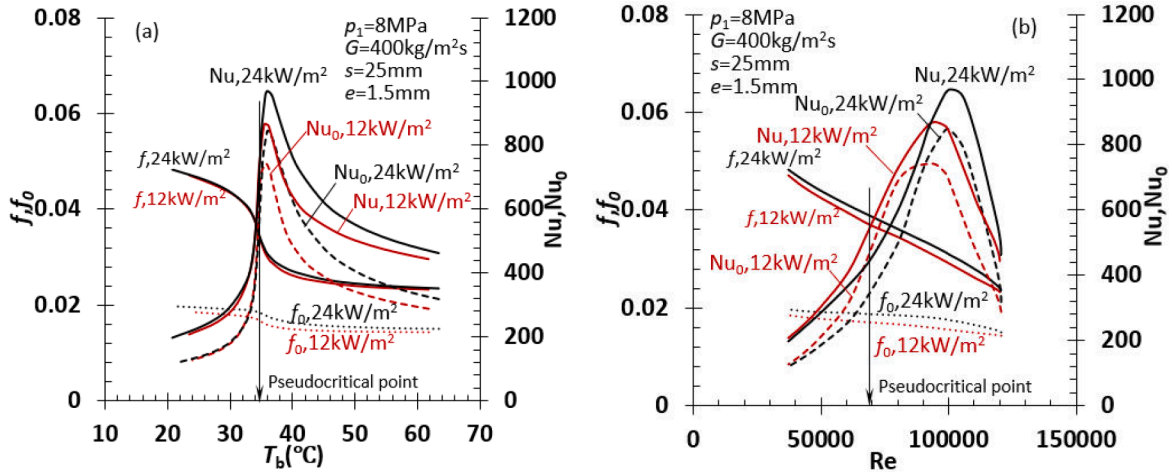
Fig. 6. Mean Nusselt number *Nu* and Darcy friction factor *f* of the EHT with *s*=25 mm and *e*=1.5 mm, mean Nusselt number *Nu*$_0$ and Darcy friction factor *f*$_0$ of the plain tube are plotted against bulk temperature *T*$_b$ (a) and nominal Reynolds number *Re* (b) at *p*$_1$=8, 9 MPa, respectively.

Fig. 7. Mean Nusselt number *Nu* and Darcy friction factor *f* of the EHT with *s*=25 mm and *e*=1.5 mm, mean Nusselt number *Nu*$_0$ and Darcy friction factor *f*$_0$ of the plain tube are plotted against bulk temperature *T*$_b$ (a) and nominal Reynolds number *Re* (b) at *q*$_w$=12, 24 kW/m^2, respectively.
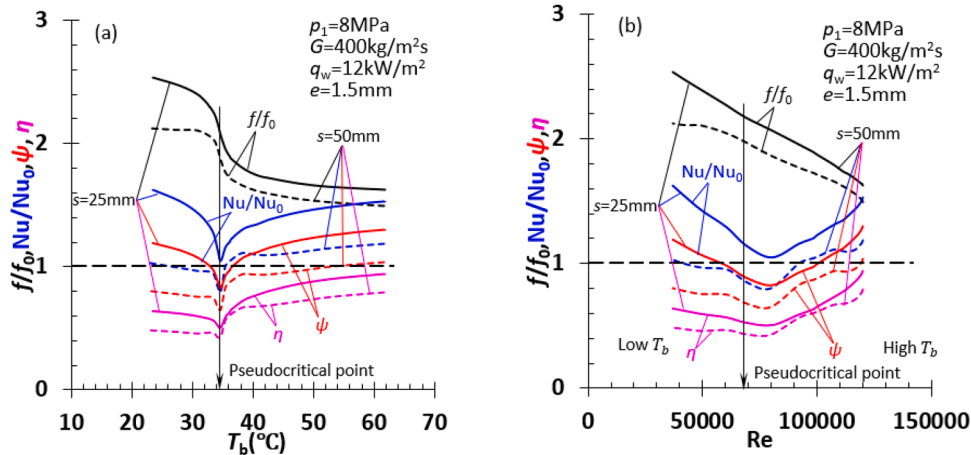
Fig. 8. *f*/*f*$_0$, *Nu*/*Nu*$_0$, ψ and η curves against *T*$_b$ (a) and *Re* (b) for the EHT with *s*=25 mm and *e*=1.5 mm at *s*=25, 50 mm.

According to Fig. 4 the effect of eccentricity on the thermal-hydraulic performance of the EHTs is negligible, and the *f*/*f*$_0$, *Nu*/*Nu*$_0$, ψ and η curves at *e*=0.9 mm overlap the curves at *e*=1.5 mm under the conditions of *G*=400 kg/m^{2}s, *p*$_1$=8 MPa, *q*$_w$=12 kW/m^2, and not demonstrated.

3.2.2. Effects of operational conditions

The operational conditions are composed of SCO2 mass flux, inlet pressure, and imposed wall heat flux. Their effects on the f/f_0, Nu/Nu_0, ψ and η curves are illustrated in Fig. 9. At a given tube diameter and SCO2 inlet temperature and inlet pressure, the nominal Reynolds number is proportional to the SCO2 mass flux. The effect of mass flux on heat transfer enhancement is equivalent to the effect of the Reynolds number on it. Basically, the mass flux demonstrates less effect on Nu/Nu_0, ψ and η than on f/f_0, especially on the left of the pseudocritical point. The EHT works more efficiently at $G=400$ kg/m²s than at $G=200$ kg/m²s in terms of ψ and η. The EHT suffers from a large f/f_0 at $G=200$ kg/m²s due to the reduced Reynolds number.

SCO2 inlet pressure can alter SCO2 pseudocritical point and nominal Reynolds number, i.e., the pseudocritical temperature rises but the nominal Reynolds number reduces with increasing inlet pressure. Generally, the heat transfer enhancement at $p_1=9$ MPa is better than at $p_1=8$ MPa in terms of Nu/Nu_0 and ψ, especially on the right of the pseudocritical point. The maximal improvement in the heat transfer enhancement at $p_1=9$ MPa is 11.3 %, 4.1 % and 7.5 % in Nu/Nu_0, ψ and η compared with the enhancement at $p_1=8$ MPa, respectively, but f/f_0 gets increased by 10 %.

A wall heat flux imposed can influence on SCO2 heat transfer enhancement in the EHT. The wall heat flux of 24 kW/m² can improve the heat transfer enhancement on the left of the pseudocritical point but
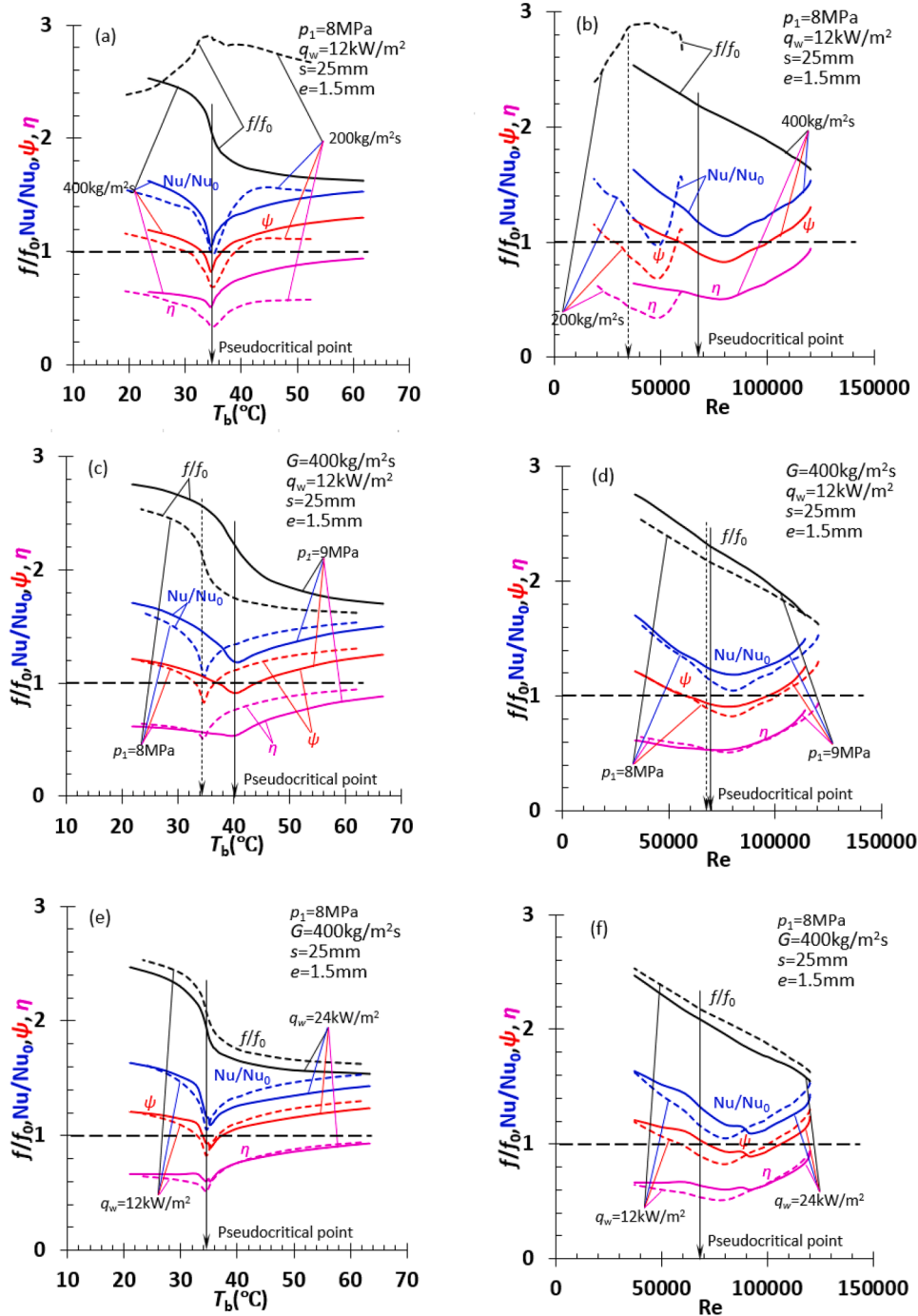

Fig. 9. f/f_0, Nu/Nu_0, ψ and η curves against T_b (left column) and against Re (right column) for the EHT with $s=25$ mm and $e=1.5$ mm at $G=200$, 400 kg/m²s (a) and (b), $p_1=8$, 9 MPa (c) and (d), $q_w=12$, 24 kW/m² (e) and (f), respectively.

reduce it on the right of the point in comparison with the heat flux of 12 kW/m^2. Interestingly, f/f_0 is smaller at the wall heat flux of 24 kW/m^2 than at the heat flux of 12 kW/m^2. For example, Nu/Nu_0, ψ and η are improved by 16.7 %, 18.1 % and 20.9 % but f/f_0 is reduced by 5.2 % at the pseudocritical point at the wall heat flux of 24 kW/m^2 compared with those at the wall heat flux of 12 kW/m^2, respectively.

3.3. Heat and fluid flow

Streamlines in the EHT and velocity contours in cross-sections of the EHT, contours of pressure, temperature, local Nusselt number and shear stress on the wall were generated to visualize SCO2 flow features and patterns and identify mechanisms of heat transfer enhancement. This will allow us to have a better understanding of heat transfer enhancement prompted by using an EHT under SCO2 flow conditions.

Fig. 10 illustrates the 3D streamlines, velocity contours in cross-sections of the EHT, contours of temperature on the wall at T_1=30, 35, 45 °C under the conditions: p_1=8 MPa, G=400 kg/m^2, q_w=12 kW/m^2, s=25 mm and e=1.5 mm. The T_1=35 °C flow condition is near the pseudocritical point. As soon as the SCO2 enters the inlet to the EHT, it starts to rotate and follow the shape of the EHT and exhibits a helical flow pattern in the tube. However, a core flow with little rotation exists near the valley of the EHT. The high-pressure zone is found on the ridge but the low-pressure zone in the valley of the tube. This effect should be associated with difference centrifugal forces acting on fluid particles near the ridge and valley of the EHT. Further, the high-temperature zone is positioned on the ridge while the low-temperature zone is shown in the valley of the tube. The flow pattern and pressure contour as well as temperature contours are little dependent on the inlet pressure of SCO2.

Fig. 11 presents the concours of local Nusselt number on the wall of the EHT and the contours of wall shear stress at T_1=30, 35, 45 °C under the conditions: p_1=8 MPa, G=400 kg/m^{2}s, q_w=12 kW/m^2, s=25 mm and e=1.5 mm. The local Nusselt number Nu_l is defined as:

$$Nu_l = \frac{h_l d}{\lambda}, \ h_l = \frac{q_w}{T_w - T_f} \tag{5}$$

where h_l, T_f, λ and T_w are local heat transfer coefficient, film temperature, i.e. wall adjacent temperature which is the average temperature in the element adjacent to the wall, thermal conductivity of SCO2 and local wall temperature, respectively, q_w is the given wall heat flux. The higher local Nusselt number is found on the ridge but the lower number is located in the valley of the EHT. This contour pattern resembles that of wall temperature.
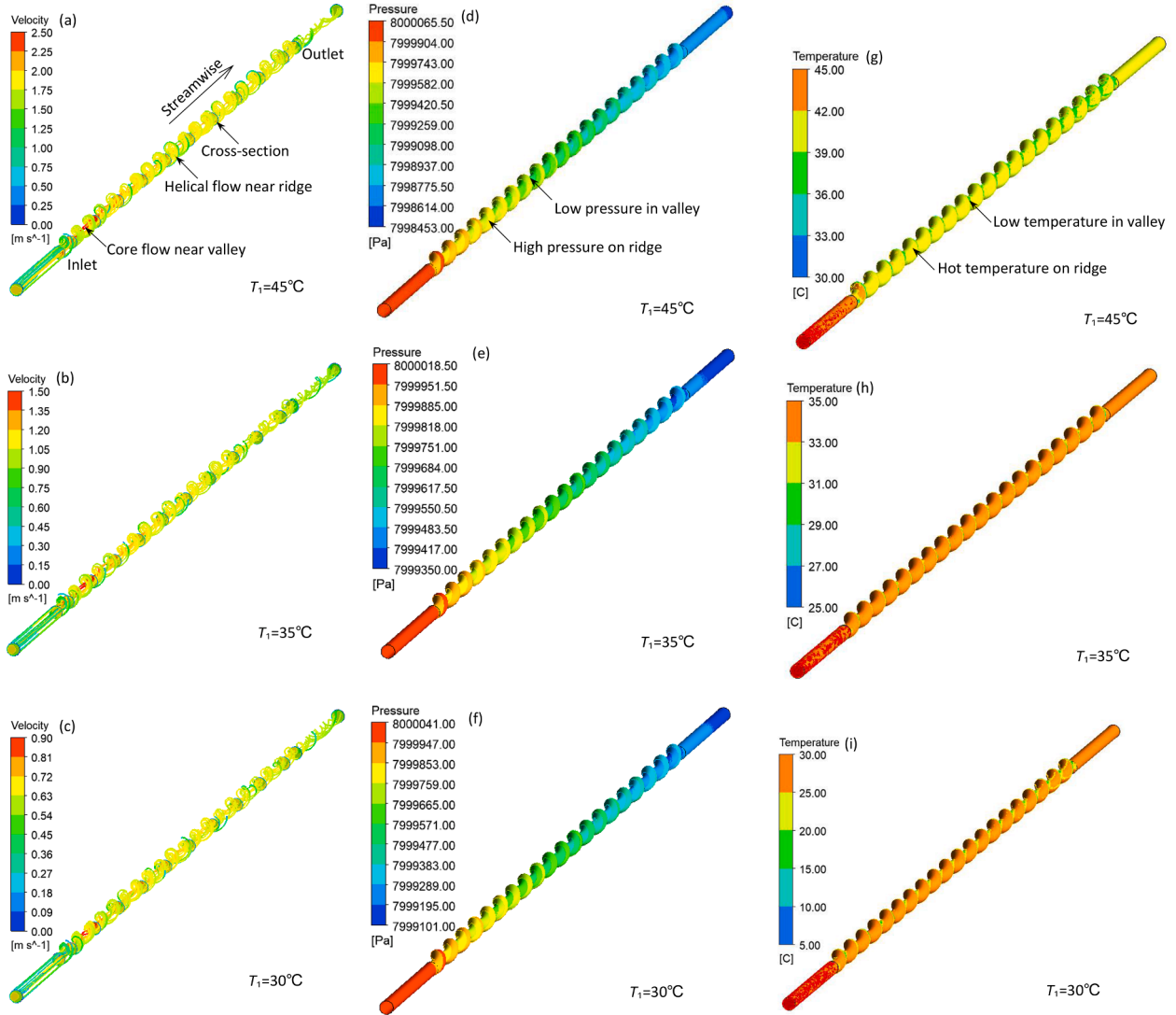

Fig. 10. Streamline and velocity contours in the inlet, outlet and ten cross-sections in the EHT and wall pressure and temperature contours at T_1=30, 35, 45 °C under the conditions of p_1=8 MPa, G=400 kg/m^{2}s, q_w=12 kW/m^2, s=25 mm and e=1.5 mm, (a)-(c) streamline and velocity contours, (d)-(f) wall pressure contours, (g)-(i) wall temperature contours, T_1=35 °C near the pseudocritical point.
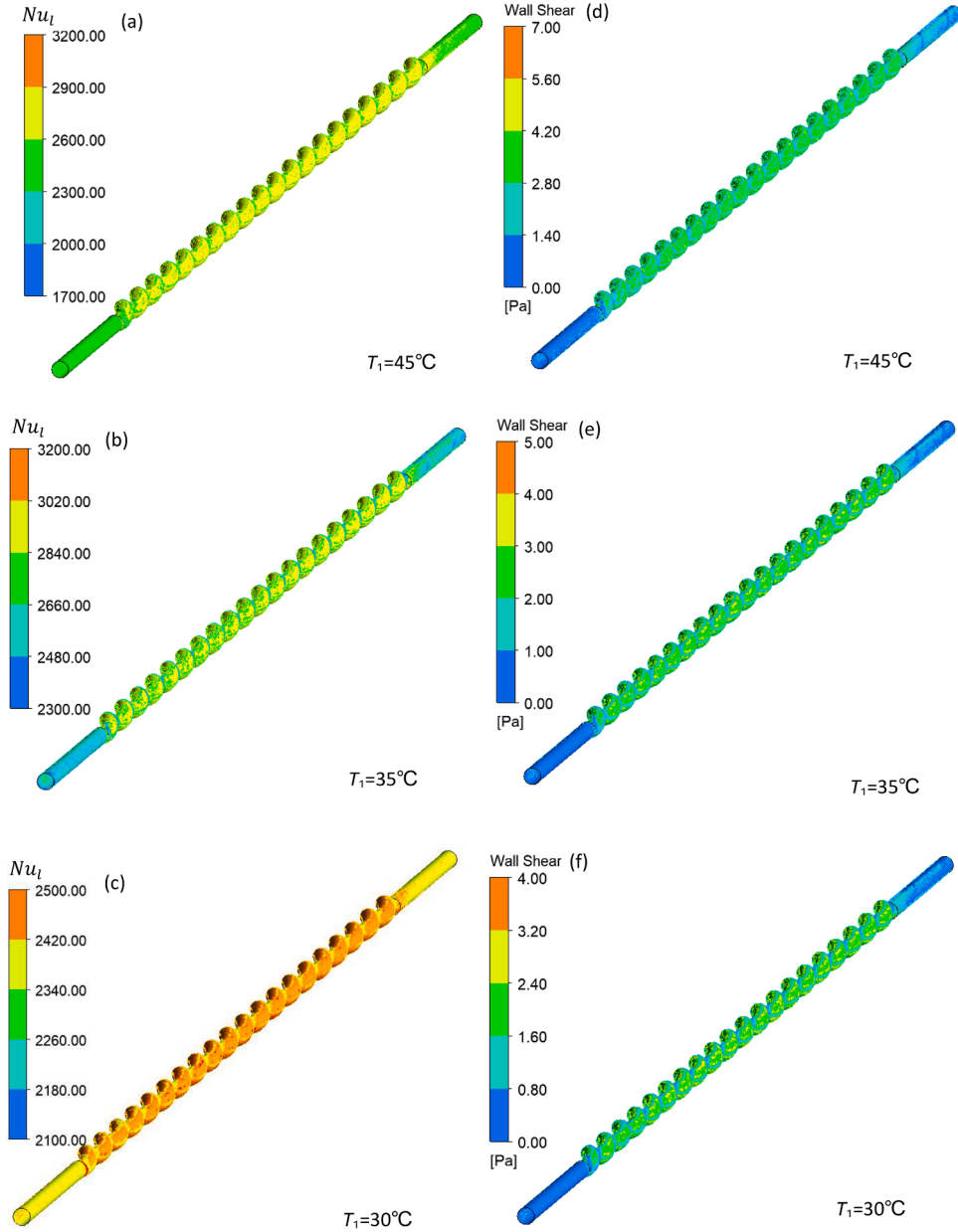
Fig. 11. Local Nusselt number and wall shear stress contours on the wall of the EHT at T_1=30, 35, 45 °C under conditions of p_1=8 MPa, G=400 kg/m²s, q_w=12 kW/m², s=25 mm and e=1.5 mm, (a)-(c) Nusselt number contours, (d)-(f) wall shear stress contours, T_1=35 °C near the pseudocritical point.

Generally, the level of wall shear stress in the EHT is significantly higher than the level of wall shear stress in the upstream and downstream extension tubes. The higher wall shear stress can also be observed on the ridge and the lower wall shear stress in the valley of the EHT. Further, the regions of higher wall shear stress match the regions of larger local Nusselt number. This matter of fact suggests that the EHT induces a helical flow of SCO2, then the flow generates a higher wall shear stress on the ridge of the tube to enhance heat transfer but inevitably experiences a greater friction loss. As a result, the higher wall temperature and Nusselt number occur on the ridge of the EHT.

3.4. Helical flow based on vortex kinetics

Absolute helicity is a useful parameter to characterize features of the streamwise helical flow induced by the twisted tape insert in a tube and can be correlated to local heat transfer coefficient on the tube wall [17]. The SCO2 velocity vector $\boldsymbol{u}$, and vorticity vector $\nabla \times \boldsymbol{u}$ are defined and

determined by [17]:

$$\boldsymbol{u} = [u_1, u_2, u_3], \nabla \times \boldsymbol{u} = \left[\frac{\partial u_3}{\partial x_2} - \frac{\partial u_2}{\partial x_3}, \frac{\partial u_1}{\partial x_3} - \frac{\partial u_3}{\partial x_1}, \frac{\partial u_2}{\partial x_1} - \frac{\partial u_1}{\partial x_2} \right] \tag{6}$$

And the absolute helicity H is defined and calculated by [17]:

$$H = |\boldsymbol{u} \cdot (\nabla \times \boldsymbol{u})| = \left| u_1 \left(\frac{\partial u_3}{\partial x_2} - \frac{\partial u_2}{\partial x_3} \right) + u_2 \left(\frac{\partial u_1}{\partial x_3} - \frac{\partial u_3}{\partial x_1} \right) + u_3 \left(\frac{\partial u_2}{\partial x_1} - \frac{\partial u_1}{\partial x_2} \right) \right| \tag{7}$$

Basically, the absolute helicity clarifies the differences in helical flows in tubes in different geometries for the same fluid at the same thermophysical and transport properties but fails to identify the differences in helical flows of fluids with different thermophysical and transport properties in the same tube.

The cross-sectional mean absolute helicity H_b of SCO2 along the EHT and local heat transfer coefficient h_l and local Nusselt number Nu_l curves against the mean absolute helicity under the conditions of p_1=8 MPa

and T_1=35 °C, p_1=9 MPa and T_1=45 °C, G=400 kg/m²s, s=25 mm, e=1.5 mm are illustrated in Fig. 12. H_b rises rapidly from the inlet (z/L=0) to the EHT, reaches a peak at z/L=0.1, then declines quickly, and finally levels off towards the outlet (z/L=1) to the tube. h_l also increases with z/L and peaks at z/L=0.05, then varies slightly towards to the outlet of the tube. This indicates that SCO2 rather quickly negotiates with the EHT and follows its shape to establish a stable helical flow.

Local heat transfer coefficient h_l and local Nusselt number Nu_l are correlated to H_b, and present in Fig. 12, too. Clearly, these two parameters can be correlated to H_b, especially for Nu_l and under the condition p_1=8 MPa and T_1=35 °C. This implies that the cross-sectional mean absolute helicity H_b is an indicator of thermal performance of an EHT for the same fluid and operational conditions.

The cross-sectional mean absolute helicity H_b of SCO2 along the EHT is shown in Fig. 13 under the conditions of p_1=9 MPa, T_1=55, 45, 35 °C, G=400 kg/m²s, s=25, 50 mm, e=0.9, 1.5 mm to clarify effects of both pitch and eccentricity H_b. Compared with s=25 mm, the H_b values are half smaller but also the peaks are delayed occurring at z/L=0.45. This means that the thermal performance such as local heat transfer coefficient and Nusselt number should be poorer than those at s=25 mm. This outcome agrees with the results shown in Fig. 4.

The H_b profiles at e=0.9 mm are almost identical to the profiles at e=1.5 mm. This suggests the helical flow in the EHT at e=0.9 mm should be nearly identical to that at e=1.5 mm in pattern but also in H_b values. Naturally, the thermal performance of the two EHTs with e=0.9, 1.5 mm should remain changed essentially. The results in Fig. 4 have reflected

this inference.

The vortex shape of helical flows in the EHT at three SCO2 inlet temperatures T_1=55, 45, 35 °C under the conditions of p_1=9 MPa, G=400 kg/m²s, q_w=12 kW/m², s=25 mm and e=1.5 mm is illustrated in Fig. 14 at three thresholds of H_b=2000, 1500, 500 m/s² for the three temperatures, respectively. The vortex shape in the figure resembles the shape of the wall of the EHT. Further, these isosurfaces match the regions with higher velocity, temperature, local Nusselt number and wall shear stress shown in Fig. 10 and Fig. 11, respectively.

4. Discussion

In this paper, four EHTs are designed in two pitches and two eccentricities, the forced convective heat transfer of SCO2 in them is simulated by using CFD software-ANSYS CFX 2019 R2 under the cooling conditions with wall heat fluxes q_w=12, 24 kW/m² at two inlet pressures p_1=8, 9 MPa and two mass fluxes G=400 kg/m²s. The thermal-hydraulic performance and four parameters for assessing heat transfer enhancement and the mechanism of heat transfer enhancement are presented and elucidated. This work is not documented in the literature currently.

In the next five sections, five prominent issues, namely effect of mass flux on friction factor, concave property in Nu/Nu_0, ψ and η curves, buoyancy effect, comparison with the other shapes of tubes and fluids, limitations and further work are debated.
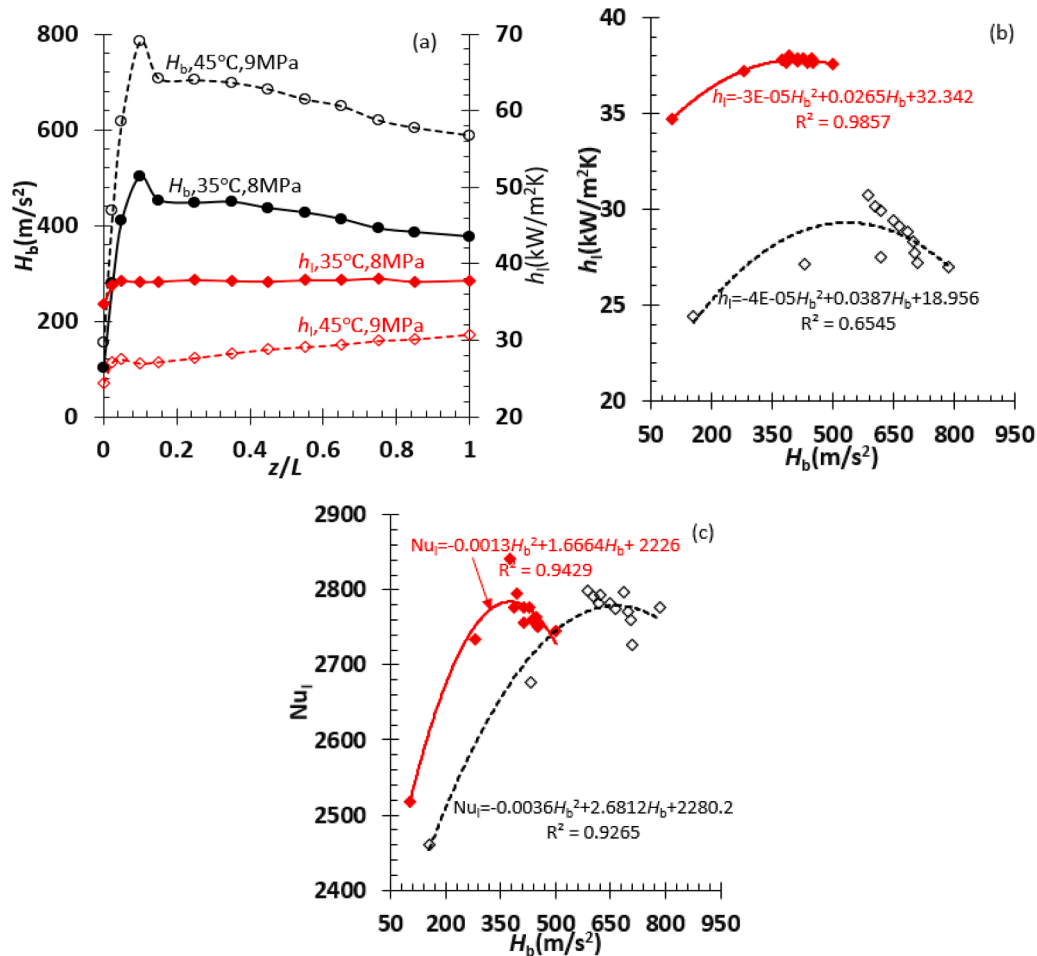

Fig. 12. Cross-sectional mean absolute helicity H_b of SCO2 is distributed along the EHT, local heat transfer coefficient h_l and local Nusselt number Nu_l are plotted against mean absolute helicity H_b under the conditions: p_1=8 MPa and T_1=35 °C, p_1=9 MPa and T_1=45 °C, G=400 kg/m²s, q_w=12 kW/m², s=25 mm, e=1.5 mm, z/L is the dimensionless axial coordinate of the EHT, z is the axial coordinate, L is the EHT length, R^2-squared correlation coefficient, (a) H_b-z/L curve, (b) h_l-H_b curve, and (c) Nu_l-H_b curve.
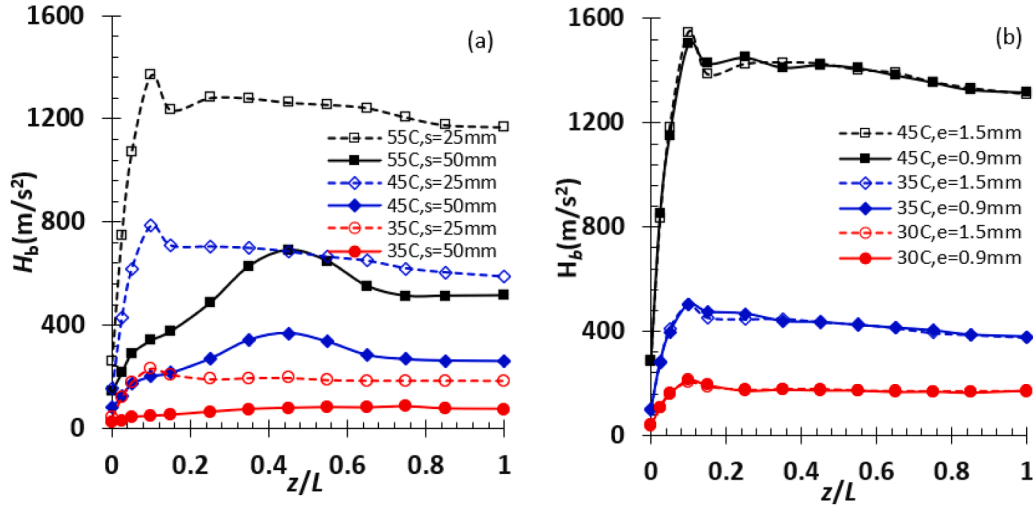
Fig. 13. Cross-sectional mean absolute helicity H_b of SCO2 varies along the EHT under the conditions: p_1=9 MPa, T_1=55, 45, 35 °C, G=400 kg/m^{2}s, q_w=12 kW/m^2, s=25, 55 mm and e=0.9, 1.5 mm, (a) s=25, 55 mm and e=1.5 mm,(b) e=0.9, 1.5 mm and, s=25 mm, z/L is the dimensionless axial coordinate of the EHT, z is the axial coordinate, L is the EHT length.
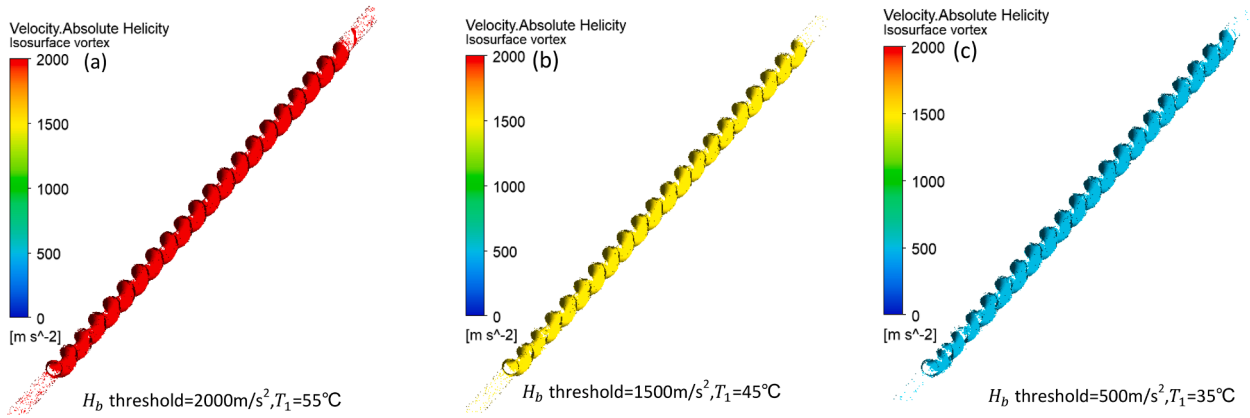

Fig. 14. Vortex shape of helical flow in the EHT at different SCO2 inlet temperatures under the conditions: p_1=9 MPa, G=400 kg/m^{2}s, q_w=12 kW/m^2, s=25 mm and e=1.5 mm, (a) T_1=55 °C and H_b threshold=2000 m/s^2, (b) T_1=45 °C and H_b threshold =1500 m/s^2, (c) T_1=35 °C and H_b threshold =500 m/s^2.

4.1. Effect of mass flux on friction factor

The f/f_0 curve declines quickly with decreasing SCO2 bulk temperature on the left of the pseudocritical point at G=200 kg/m^{2}s as shown in Fig. 9(a) and (b). To confirm this phenomenon is relevant to mass flux only, two cases of G=200, 400 kg/m^{2}s at p_1=9 MPa was launched and the corresponding four parameters are present in Fig. 15. The same phenomenon in the f/f_0 curve as demonstrated in Fig. 9(a) and (b) at p_1=8 MPa remerges at p_1=9 MPa. This fact suggests that the phenomenon has nothing to do with SCO2 inlet pressure but its mass flux. Snice the friction factor is mainly related to SCO2 dynamic viscosity, the ratio of the SCO2 bulk dynamic viscosity μ_b in the EHT to the bulk dynamic viscosity μ_{b0} in the plain tube at every inlet temperature is calculated based on the CFD simulation results in each case, and illustrated in Fig. 15(c). The peak as high as 1.15 and subsequent dramatic recline in ratio μ/μ_0 at G=200 kg/m^{2}s should be responsible for the phenomenon.

4.2. Concave property in Nu/Nu_0, ψ and η curves

There is a concave property in Nu/Nu_0, ψ and η curves as shown in Figs. 8 and 9. The concave property manifests itself in that a valley exists in Nu/Nu_0, ψ and η curves near the pseudocritical point and the depth of the valley decreases with the increasing mass flux. First, it is suspected

that this valley is relevant to hybrid and conservative options in extracting the averaged wall temperature in CFX-Post. When the values of some primary variables of fluid, e.g., velocity, temperature, density and dynamic viscosity, enthalpy and entropy at a wall are calculated in CFX-Post, an algorithm, i.e., hybrid option or conservative option needs to be specified [31]. The hybrid option was selected in CFX-Post to calculate the value of a variable at a wall in the paper. To examine the effect of hybrid and conservative options on the result of heat transfer enhancement, the conservative option is activated under the conditions: p_1=9 MPa, G=400 kg/m^{2}s, q_w=12 kW/m^2, s=25 mm, and e=1.5 mm, and Nu/Nu_0, ψ and η values are recalculated, the ψ value, wall temperature difference ΔT_{ch} and relative error in mean heat transfer coefficient $\Delta h/h$ between conservative option and hybrid option are illustrated against inlet temperature T_1 in Fig. 16. The values of Nu_0 were calculated by using the parameters extracted with the conservative option in CFX-Post as well. It is shown that the conservative option raises wall temperature by 0.30–0.84 K, resulting in h and ψ increased by 7.72–24.33 %. However, the shape of the ψ curve is independent of hybrid or conservative option.

The shape of Nu/Nu_0 and ψ curves of twisted tape insert is convex near the pseudocritical point under SCO2 turbulent flow conditions in [17], indicating the best heat transfer enhancement near the pseudocritical point. However, their shape in this paper is concave at the
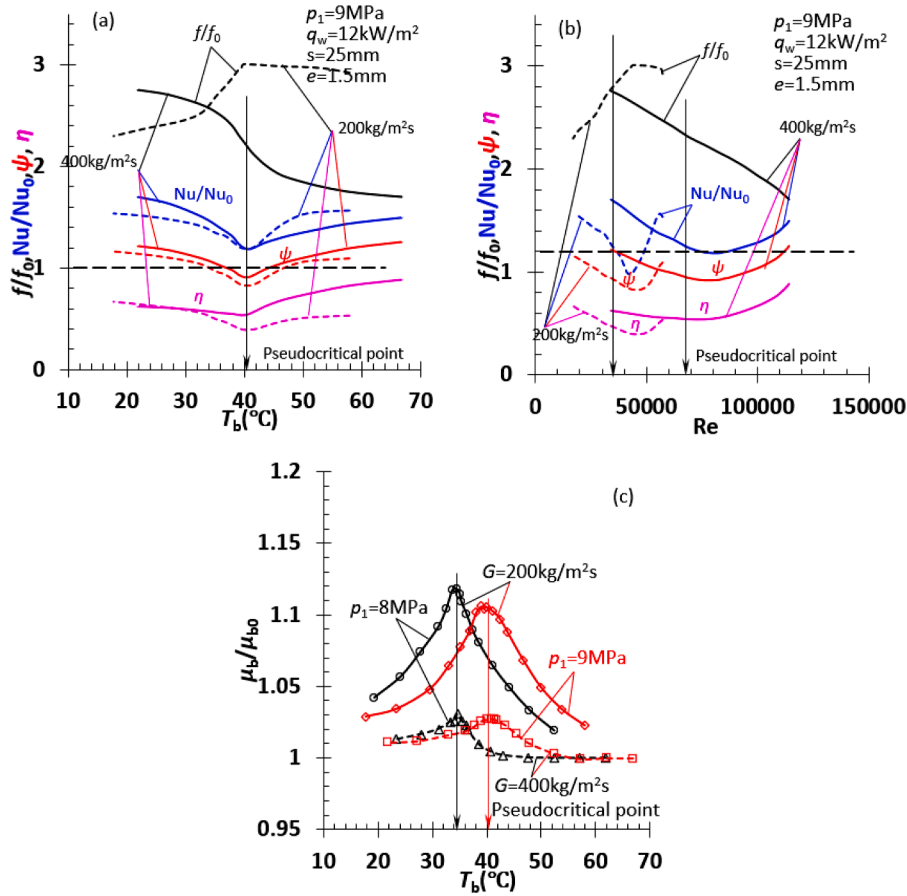
Fig. 15. f/f_0, Nu/Nu$_0$, ψ and η curves against T_b (a) and Re (b) for the EHT with s=25 mm and e=1.5 mm at $G = 200, 400$ kg/m^{2}s and p_1= 9 MPa, the bulk dynamic viscosity ratio μ/μ_0 of SCO2 versus bulk temperature T_a (c) at two mass fluxes and two inlet pressures.
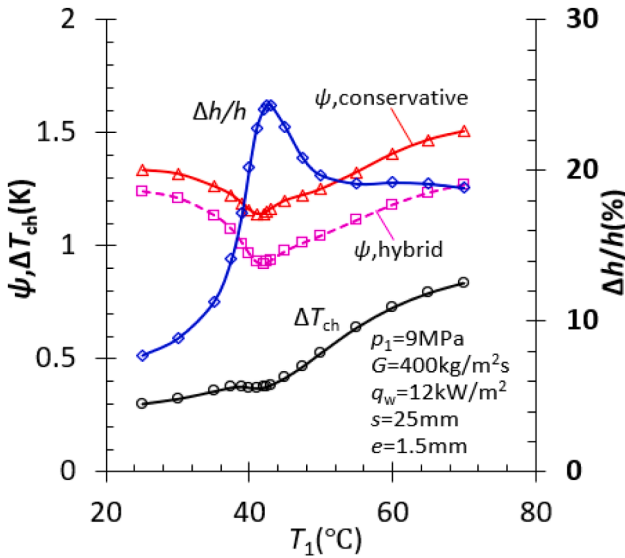

Fig. 16. ψ value, wall temperature difference ΔT_{ch} and relative error in the mean heat transfer coefficient $\Delta h/h$ between conservative option and hybrid option against inlet temperature T_1 under the condition of p_1=9 MPa, G=400 kg/m^{2}s, q_w=12 kW/m^2, s=25 mm and e=1.5 mm.

pseudocritical point, suggesting the poorest heat transfer enhancement near the point. Obviously, the conservative option does not alter this concave property of Nu/Nu_0 and ψ curves.

Second, it is supposed that the occurrence of the valley in the curves

may be associated with variation of the Prandtl number, because Nusselt number of a convective heat transfer usually depends on Prandtl number. The ratios of the SCO2 bulk Prandtl number Pr_b, specific heat capacity at constant pressure c_p, and thermal conductivity λ_b in the EHT to the bulk Prandtl number Pr_{b0}, specific heat capacity at constant pressure c_{p0}, and thermal conductivity λ_{b0} in the plain tube are extracted from CFD simulation results at p_1=8, 9 MPa, G=200, 400 kg/m^{2}s, q_w=12 kW/m^2, s=25 mm and e=1.5 mm and plotted against the bulk temperature T_b in Fig. 17. The SCO2 bulk Prandtl number Pr_b in the EHT and the bulk Prandtl number Pr_{b0} in the plain tube are defined as:

$$P_{rb} = \frac{c_{pb}\mu_b}{\lambda_b}, \; P_{rb0} = \frac{c_{pb0}\mu_{b0}}{\lambda_{b0}} \tag{8}$$

where c_{pb}, μ_b and λ_b denote the bulk specific heat capacity at constant pressure, dynamic viscosity and thermal conductivity of SCO2 in the EHT, c_{pb0}, μ_{b0} and λ_{b0} are the counterpart in the plain tube. A significant decline in Pr$_b$/Pr$_{b0}$ is observed near the pseudocritical point, especially at G=200 kg/m^{2}s. The reduction in Pr$_b$/Pr$_{b0}$ is essentially attributed to the reduction in c_p/c_{p0} rather than λ_b/λ_{b0}.

4.3. Explanation of effect of wall heat flux

In Fig. 9, the increase of wall heat flux can improve heat transfer enhancement on the left side (low inlet temperature) but weaken it on the right side (high inlet temperature) of the pseudocritical point. Additionally, the friction ratio f/f_0 is smaller at q_w=24 kW/m^2 than at q_w=12 kW/m^2. These two phenomena may relate to SCO2 thermosphysical properties at wall. The SCO2 wall temperature and SCO2 bulk temperature as well as temperature difference between bulk
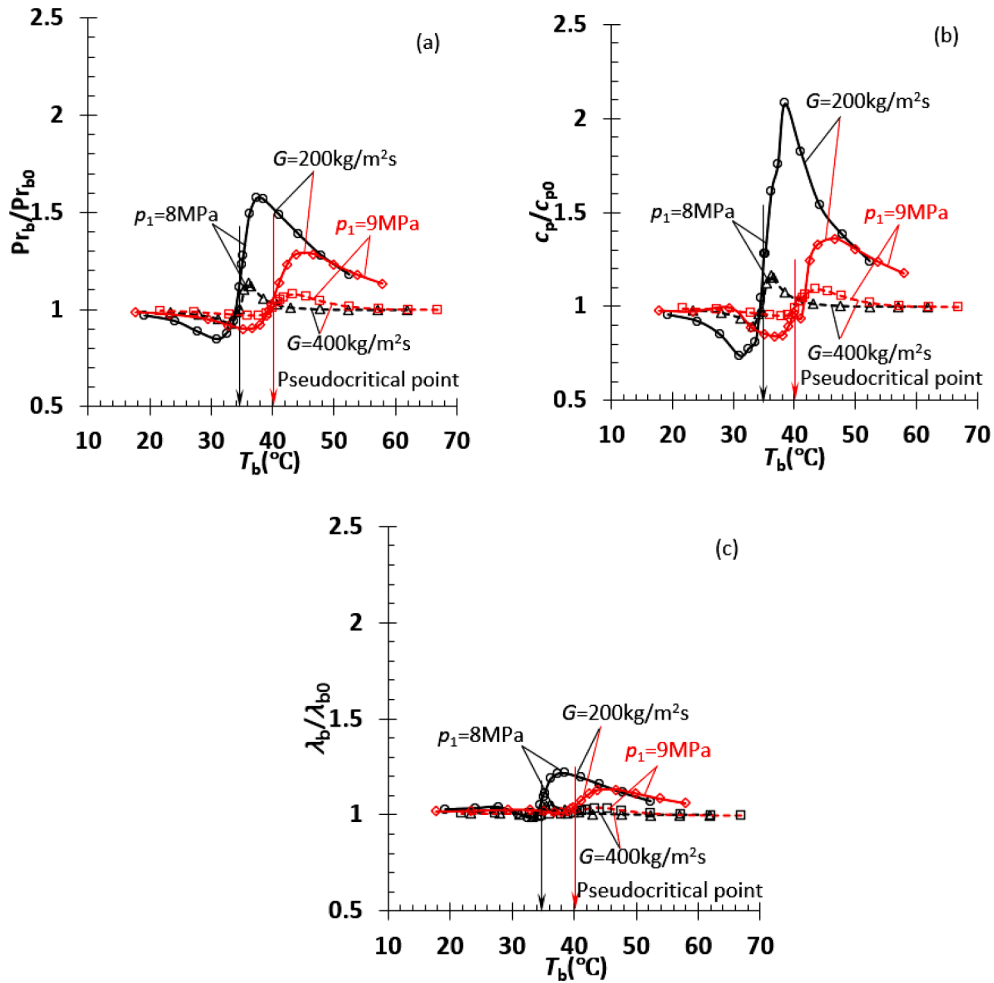
Fig. 17. Ratios of the SCO2 bulk Prandtl number Pr_b, specific heat capacity at constant pressure c_p, and thermal conductivity λ_b in the EHT to the Prandtl number Pr_{b0}, specific heat capacity at constant pressure c_{p0}, and thermal conductivity λ_{b0} in the plain tube versus the bulk temperature T_b at p_1=8, 9 MPa, G=200, 400 kg/m²s, q_w=12 kW/m², s=25 mm and e=1.5 mm, (a) Pr_b/Pr_{b0}, (b) c_p/c_{p0}, and (c) λ_b/λ_{b0}.

temperature and wall temperature at the two wall heat fluxes are illustrated Fig. 18. The SCO2 bulk temperature rises with increasing SCO2 inlet temperature on both the sides of the pseudocritical point but in different slopes. At a given inlet temperature, the bulk temperature at q_w=24 kW/m² is slightly lower than at q_w=12 kW/m². At the pseudocritical point, however, the bulk temperature is irrelevant to wall heat flux, and thus the temperature remains unchanged.

The wall temperature largely depends on wall heat flux. At a fixed inlet temperature, the larger the wall heat flux, the lower the wall temperature in the plain tube and the EHT, respectively. The wall temperature rises with SCO2 inlet temperature, especially on the left side of the pseudocritical point. At a fixed inlet temperature, the wall temperature of the EHT is higher than the wall temperature of the plain tube. At the pseudocritical point, the wall temperature shows negligible variation in the plain tube and the EHT at a wall heat flux.

The temperature difference between bulk temperature and wall temperature is considerably dependent on SCO2 inlet temperature and wall heat flux. The temperature difference declines towards the pseudocritical point or vice versus. The temperature difference at q_w=24 kW/m² is smaller than the difference at q_w=12 kW/m² in the plain tube or EHT at a given inlet temperature. At a fixed wall heat flux, the temperature difference in the EHT is smaller than the temperature difference in the plain tube, indicating the occurrence of heat transfer enhancement at an inlet temperature, especially on the left side of the pseudocritical point.

The temperature difference exhibits a slight variation from the EHT

to the plain tube near the pseudocritical point but a gradually notable change away from that point, suggesting marginal heat transfer enhancement near the point but substantial heat transfer enhancement away from that point. As a result, a concave property in Nu/Nu_0, ψ and η curves is shown in Figs. 8 and 9. The SCO2 thermal conductivity at wall in the plain tube and EHT is demonstrated in Fig. 19(a). The thermal conductivity near the pseudocritical point varied slightly from the plain tube to the EHT in comparison with both the sides of the point. Therefore, the temperature differences $T_b - T_w$ and $T_{b0} - T_{w0}$ should demonstrate an minor change near the pseudocritical point in the EHT and plain tube.

The Prandtl number at wall in the plain tube and EHT is illustrated in Fig. 19(b). The Prandtl number at wall in the EHT on the left side (low inlet temperature) of the pseudocritical point is higher, but the number on the right side (high inlet temperature) of the point is lower than the number in the plain tube at a given inlet temperature, especially at q_w=24 kW/m². This matter of fact implies that the increasing wall heat flux can enhance heat transfer more on the left side but less on the right side of the pseudocritical point.

The SCO2 dynamic viscosity and shear stress at wall in the plain tube and EHT are given in Fig. 20. The dynamic viscosity at wall in the EHT is smaller than the viscosity in the plain tube, especially at q_w=24 kW/m² for a given inlet temperature. Furthermore, the dynamic viscosity at q_w=24 kW/m² is significantly larger than the viscosity at q_w=12 kW/m² in the plain tube. Accordingly, the shear stress at wall at q_w=24 kW/m² is higher than the stress at q_w=12 kW/m² in the pain tube, while the
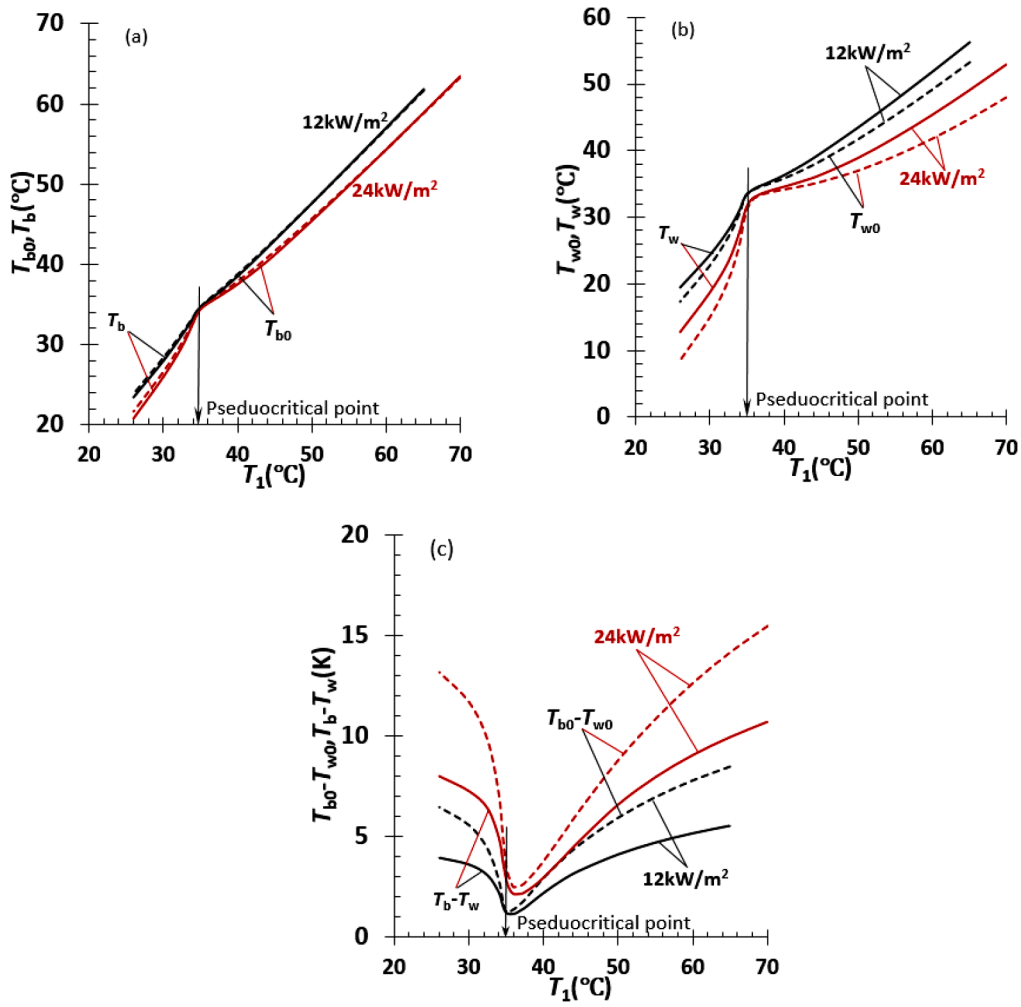
Fig. 18. Wall temperature and SCO2 bulk temperature as well as difference between bulk temperature and wall temperature are plotted as a function of SCO2 inlet temperature in the EHT and plain tube under the conditions of s=25 mm, e=1.5 mm, $G = 400$ kg/m²s, p_1=8 MPa, q_w=q_{w0}=12, 24 kW/m², respectively, (a) bulk temperatures T_{b0} in the plain tube and T_b in the EHT, (b) wall temperatures T_{w0} of the plain tube and T_w of the EHT, (c) temperature differences between bulk temperature and wall temperature T_{b0}-T_{w0} in the plain tube and T_b-T_w in the EHT.
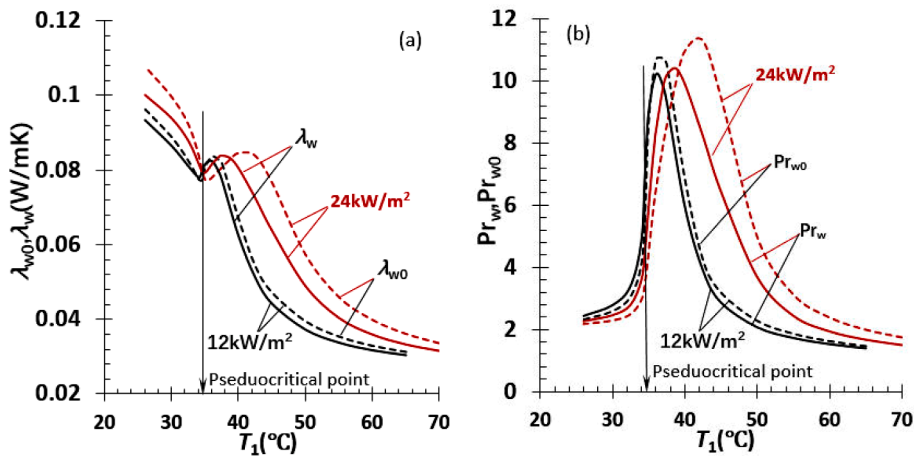

Fig. 19. SCO2 thermal conductivity and Prandtl number at wall are plotted as a function of SCO2 inlet temperature in the EHT and plain tube under the conditions of s=25 mm, e=1.5 mm, $G = 400$ kg/m²s, p_1=8 MPa, q_w=q_{w0}=12, 24 kW/m², respectively, (a) thermal conductivities λ_{w0} in the plain tube and λ_w in the EHT, (b) Prandtl numbers Pr_{w0} in the plain tube and Pr_w in the EHT.
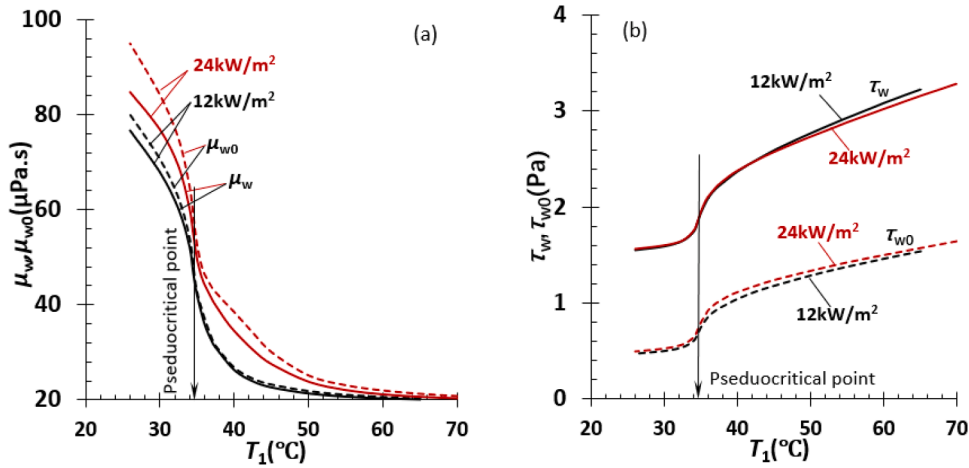
Fig. 20. SCO2 dynamic viscosity and shear stress at wall are plotted as a function of SCO2 inlet temperature in the EHT and plain tube under the conditions of s=25 mm, e=1.5 mm, G = 400 kg/m²s, p_1=8 MPa, q_w=q_{w0}=12, 24 kW/m², respectively, (a) dynamic viscosities μ_{w0} in the plain tube and μ_w in the EHT, (b) Prandtl numbers Pr_{w0} in the plain tube and Pr_w in the EHT.

shear stress at wall at q_w=24 kW/m² is lower than the stress at q_w=12 kW/m². Thus, the friction ratio f/f_0 is lower at q_w=24 kW/m² than at q_w=12 kW/m².

4.4. Buoyancy effect

Buoyancy effect may exist in convective heat transfer of SCO2 in a cooled horizontal tube. The effect depends on Richardson number Ri, which is defined and calculated by [29]:
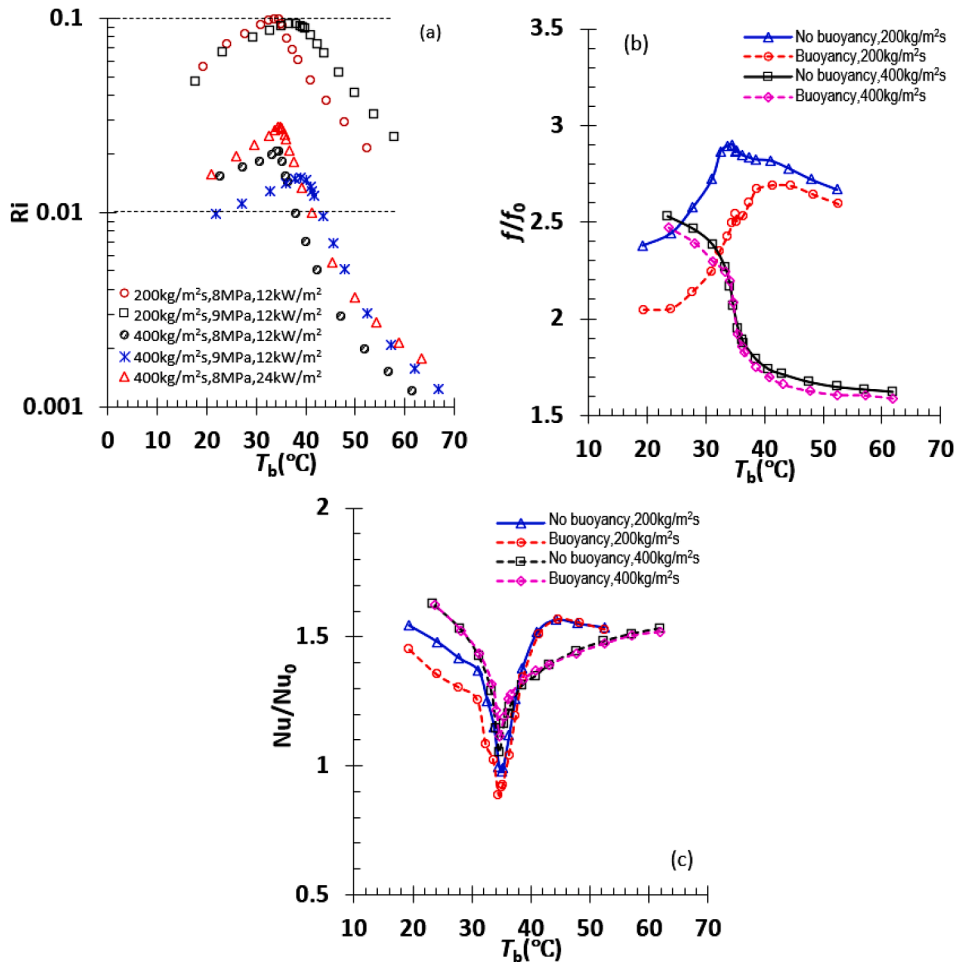

Fig. 21. Richardson number Ri versus SCO2 bulk temperature T_b in five cases studied, and comparison of f/f_0 and Nu/Nu_0 curves with and without buoyancy effect at G=200, 400 kg/m²s, p_1=8 MPa, q_w=12 kW/m², (a) Richardson number curves, (b) f/f_0 curves, (c) Nu/Nu_0 curves.

$$Ri = \frac{(\rho_w - \rho_b)\rho_b g d}{G^2} \qquad (9)$$

where ρ_w is SCO2 density at tube wall, g is the acceleration of gravity, g=9.81 m/s². The natural heat transfer induced by the buoyancy effect should be neglected at $Ri<0.001$ [32]. If $0.01<Ri<0.1$ is true, the buoyancy effect will play a role in SCO2 convective heat transfer in a cooled horizontal tube [33]. If $0.1<Ri<10$ is held, the buoyancy must be considered in the convective heat transfer of SCO2 [34,35]. The range of Ri in five cases is shown in Fig. 21. The Ri values have reached 0.1 at G=200 kg/m²s but far below 0.1 at G=400 kg/m²s. The buoyancy effect should be stronger at G=200 kg/m²s than that at G=400 kg/m²s.

Four cases (two for the EHT, two for the plain tube) with buoyancy effect were simulated under the conditions of G=200, 400 kg/m²s, p_1=8 MPa, q_w=12 kW/m², g_1=g_3=0, g_2=9.81 m/s², ρ_{ref}=483.82 kg/m³ with the Boussinesq approximation [36] and the corresponding ratios f/f_0 and Nu/Nu_0 curves against T_b are illustrated in Fig. 21(b) and (c). The f/f_0 and Nu/Nu_0 values are affected so little that the buoyancy effect can be ignored at G=400 kg/m²s. The f/f_0 values are influenced greatly by the buoyancy effect in a wide range of T_b, but Nu/Nu_0 varies considerably on the left of the pseudocritical point at G=200 kg/m²s. Mostly, the heat transfer enhancement results in the paper are achieved at G=400 kg/m²s and they are reliable in regarding to the buoyancy effect.

4.5. Comparison with the other shapes of tube and fluids

The forced convective heat transfer enhancement of SCO2 in the EHT under the conditions of T_1=26–65 °C, p_1=8 MPa, G=400 kg/m²s, s=25 mm and e=1.5 mm is compared with that of air in the EHTs [24], water in the twisted elliptical tubes (TET) [37,38] and conical tube (CT) [13]. The corresponding parameters f/f_0, Nu/Nu_0, ψ and η for assessing heat transfer enhancement are illustrated in Fig. 22 against nominal Reynolds number Re. As shown in Fig. 22(a), the shape of the f/f_0, Nu/Nu_0, ψ and η curves versus the Reynolds number of SCO2 on the left of the pseudocritical point is similar to air in the EHTs but differs from that of air on the right of the point. Since the four parameters decrease with increasing Reynolds number, and the Reynolds number of the SCO2 flowing the EHT is ten times higher than the air, the four parameters of SCO2 is smaller than those of the air overall. However, the heat transfer enhancement is improved with increasing Reynolds number on the right side of the point. This unique feature of SCO2 across the pseudocritical point in heat transfer enhancement requires further experimental investigation in the future.

Compared with the experimental [37] and CFD simulated [38] data of the four parameters of water in the TET as show in Fig. 22(b), The EHT in SCO2 turbulent flow condition exhibits a larger f/f_0, comparable Nu/Nu_0 and ψ, but a lower η. In contrast to the four parameters of water in the CT predicted by CFD simulation [13], the EHT in the SCO2 turbulent flow condition demonstrates a smaller f/f_0, comparable Nu/Nu_0 and ψ, and better η.

Even though a CT can have a considerably better Nu/Nu_0 value at a higher Reynolds number in Fig. 22(b), the f/f_0 value approaches to f/f_0=5 with increasing Reynolds number. When a passive method for heat transfer enhancement is assessed, the ratio f/f_0 must be considered [39]. It is proposed that f/f_0=5 is a critical value. If $f/f_0>5$ is true for a passive method, the method can result in a serious pressure drop. Or if $f/f_0\leq5$ is valid for a passive method, the method can induce an acceptable pressure drop and is applicable to heat transfer enhancement in a tube. Based on the f/f_0=5 critical value, the CT is unsuitable to the heat transfer enhancement in a tube at a Reynolds number higher than 10^5. The f/f_0 value of the EHT appears to be in between the TET and the CT while the Nu/Nu_0 and ψ values are comparable among them.

4.6. Limitation and further work

The paper is subject to three limitations. First, the CFD simulation results of heat transfer enhancement and friction factor of SCO2 in the EHTs are not validated and supported by any experimental data. Hopefully, experimental work on friction factor and heat transfer of SCO2 in the EHTs can be conducted in our laboratory in the future. Second, the predicted concave property in Nu/Nu_0, ψ and η curves should be confirmed or denied experimentally in the future. Third, the helical flow pattern and flow details of SCO2 in the EHTs need to be revealed experimentally in the future.

Very recently, a matter of fact was established experimentally that there was an imposed wall heat flux by which the maximal local heat transfer coefficient could be achieved longitudinally for SCO2 flowing in uniformly heated horizontal [40] or vertical [41] miniature tubes. However, this phenomenon was not identified in SCO2 forced convective heat transfer in cooled horizontal tubes in a diameter of 6 mm [27]. Thus, two experimental wall heat fluxes of 12 and 24 kW/m² in [27] were adopted in our CFD simulations. Nonetheless, the effect of the other experimental heat fluxes such as 6 and 33 kW/m² in [27] on SCO2 heat transfer enhancement are worth being clarified in the future.

The buoyancy effect on heat transfer enhancement of SCO2 at a mass flux lower than 200 kg/m²s is worth being investigated. To strengthen
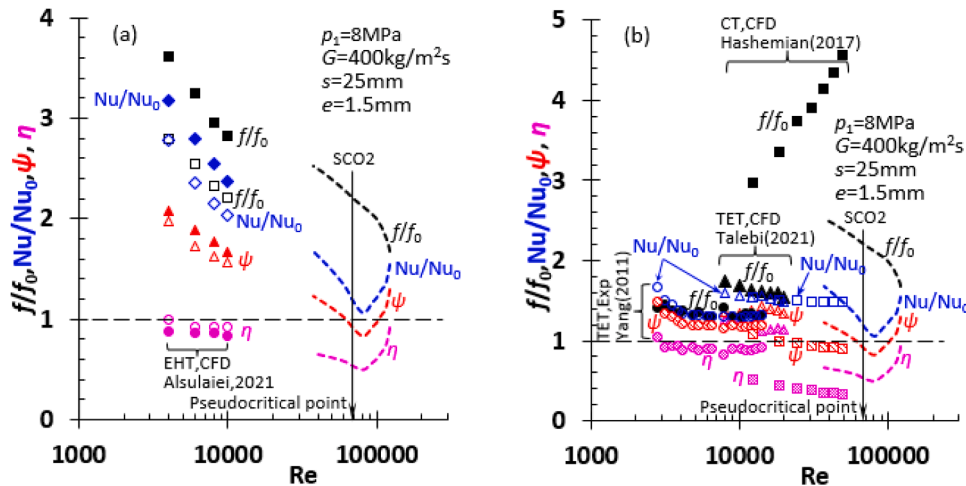
Fig. 22. f/f_0, Nu/Nu_0, ψ and η of SCO2 in the EHT under the conditions of T_1=26–65 °C, p_1=8 MPa, G=400 kg/m²s, s=25 mm and e=1.5 mm are compared with those of air in the EHT, water in the twisted elliptical tubes (TET) and conical tube (CT), respectively, (a) compared with air in the plain EHT and the EHT with one twisted tape attached to the wall in [24], where solid symbols-the EHT with the tape, open symbols-the plain EHT, (b) compared with water in the TETs [37,38] and CT [13], where circles-experimental data [37], triangles-CFD simulations [38], and squares-CFD simulations [13].

understanding of the mechanism of heat transfer enhancement achieved by EHTs, field synergy [42], entropy generation analysis [43] and second law analysis [44] on convective heat transfer of SCO2 in the EHTs are on demand.

This article is devoted to the thermal-hydraulic performance and heat and fluid flow only, the other issues such as EHT manufacturing and nonuniform stress and strain developed in the EHT wall at an internal pressure as high as 8–10 MPa need to be addressed in the future.

5. Conclusion

Three eccentrical helical tubes with pitches of 25, 50 mm and eccentricities of 0.9, 1.5 mm were designed. The convective heat transfer of SCO2 flowing in those tubes and the corresponding plain tube was simulated by using the three-dimensional steady Reynolds-averaged Navier-Stokes equations and shear stress transport turbulence model in ANSYS CFX 2019 R2 at mass fluxes of 200, 400 kg/m^{2}s, inlet pressures of 8, 9 MPa, outwards wall heat fluxes of 12, 24 kW/m^2. The flow and heat transfer models were validated in the plain tube with experimental data on mean heat transfer coefficient and empirical correlations for friction factor found in the literature. Quantitative results of heat transfer enhancement achieved by the eccentrical helical tubes, and influences of pitch and eccentricity as well as operational conditions on the enhancement were clarified. The flow pattern, heat transfer detail and vortex identification were analysed. The heat transfer enhancement of SCO2 in the eccentrical helical tubes was compared with that of water or air in eccentrical helical tubes, twisted elliptical tubes and conical tubes in the literature.

It turns out that the pitch demonstrates a stronger influence on the thermal-hydraulic performance of eccentrical helical tubes than the eccentricity in SCO2 turbulent flow regimes. The 25 mm pitch (4.17 pitch ratio) and 1.5 mm eccentricity (0.25 eccentricity ratio) are a better choice for the eccentrical helical tube targeted in the paper.

A higher SCO2 mass flux increases Nusselt number but reduces friction factor evidently. The eccentrical helical tube operates more efficiently at G=400 kg/m^{2}s than at G=200 kg/m^{2}s based on ψ and η. SCO2 inlet pressure affects Nusselt number more notably than friction factor, and with increasing inlet pressure the peaks in Nusselt number curves decline and the curves attempt to be flattened. Wall heat flux influences Nusselt number more greatly than friction factor, especially the larger the heat flux, the larger the Nusselt number and the greater the friction factor. f/f_0 reduces with increasing inlet pressure and nominal Reynolds number in the range of 2.52–1.68, and Nu/Nu_0, ψ and η curves decline towards the pseudocritical point and exhibit a concave shape, their values are ranged in 1.68–1.06 and 1.06–1.55, 1.23–0.83 and 0.83–1.30, 0.67–0.50 and 0.50–0.92 at s=25 mm, e=1.5 mm, p_1=8 MPa, G=400 kg/m^{2}s, and q_w=12 kW/m^2, respectively. Compared with the inlet pressure of 8 MPa, the maximal improvement of heat transfer enhancement at the inlet pressure of 9 MPa is 11.3 %, 4.1 %, 7.5 % in Nu/Nu_0, ψ, and η but along with a 10 % increase of f/f_0. f/f_0 reduces with

increasing wall heat flux, Nu/Nu_0, ψ and η are enhanced by 16.7 %, 18.1 % and 20.9 % but f/f_0 is smaller by 5.2 % at the wall heat flux of 24 kW/m^2 than at the flux of 12 kW/m^2 at the pseudocritical point.

SCO2 exhibits a helical flow pattern with a core flow in the eccentrical helical tube, the high-pressure, high-temperature, high-Nusselt number and high-shear stress regions are all located on the ridge while the low-pressure, low-temperature, low-Nusselt number and low-shear stress regions occur in the valley of the tube. The heat transfer enhancement is attributed to a higher wall shear stress on the ridge of the tube. The local heat transfer coefficient can be correlated to the absolute helicity, and the vortex flow is identified by using absolute helicity, the high absolute helicity regions match the high-wall shear stress regions.

The concave shape/property near the pseudocritical point in Nu/Nu_0, ψ and η curves is relevant to the remarked reduction in Pr_b/Pr_{b0} near the point, especially at G=200 kg/m^{2}s. The f/f_0 value of the eccentrical helical tube is in between the twisted elliptical tube and the conical tube, but the Nu/Nu_0 and ψ values are comparable among them, and the conical tube is unlikely applicable to the heat transfer enhancement in a tube at a Reynolds number beyond 10^5 according to the f/f_0=5 criterion.

Experimental study on friction factor and heat transfer of SCO2 and confirmation of concave property in Nu/Nu_0, ψ and η curves in eccentrical helical tubes are desirable and should be performed in our laboratory in the future.

CRediT authorship contribution statement

Wenguang Li: Conceptualization, Investigation, Methodology, Formal analysis, Visualization, Writing – original draft. **Zhibin Yu:** Methodology, Writing – review & editing, Funding acquisition, Project administration.

Declaration of Competing Interest

The authors declare that they have no known competing financial interests or personal relationships that could have appeared to influence the work reported in this paper.

Data availability

Data will be made available on request.

Acknowledgement

Appendix A. Flow and Heat Transfer Models and Validation

A1. Flow and heat transfer models

For the three-dimensional, steady, subsonic, compressible SCO2, RANS equations and energy equation with eddy viscosity turbulence models are written as [36]

$$\frac{\partial}{\partial x_j}\left(\rho u_j\right) = 0 \tag{A.1}$$

$$\frac{\partial}{\partial x_j}\left(\rho u_i u_j\right) = -\frac{\partial}{\partial x_i}\left(p + \frac{2}{3}\rho k\right) + \frac{\partial}{\partial x_j}\left[\left(\mu + \mu_t\right)\left(\frac{\partial u_i}{\partial x_j} + \frac{\partial u_j}{\partial x_i}\right)\right] + \rho g_i \tag{A.2}$$

$$\frac{\partial}{\partial x_j}\left[\rho u_j\left(\hbar +\frac{1}{2}u_iu_i+k\right)\right]=\frac{\partial}{\partial x_j}\left(\lambda\frac{\partial T}{\partial x_j}+\frac{\mu_t}{Pr_t}\frac{\partial \hbar}{\partial x_j}\right)+S_E \tag{A.3}$$

where ρ is the density of SCO2, u_i and u_j are the Reynolds-averaged velocity components of SCO2 in the coordinate x_i and x_j directions, respectively; i and j are the coordinate index, i, j=1, 2, 3; p is the static pressure of SCO2, k is the turbulent kinetic energy, $k=\frac{1}{2}\overline{u_i'^2}$, u_i' is turbulent fluctuation velocity components of SCO2, μ is the dynamic viscosity of SCO2, μ_t is the turbulent eddy viscosity, g_i is the specific body force, g_i=0 is held here, $\hbar$ is the enthalpy of SCO2, λ is the thermal conductivity of SCO2, T is the temperature of SCO2, Pr_t is the turbulent Prandtl number, Pr_t=0.85, S_E is the source term of energy, S_E=0 here; ρ, μ and λ are interp0lated by the real gas property table.

The Wilcox k-ω turbulence model is written as [36]:

$$\frac{\partial}{\partial x_j}\left(\rho u_j k\right)=\frac{\partial}{\partial x_j}\left[\left(\mu+\frac{\mu_t}{\sigma_{k1}}\right)\frac{\partial k}{\partial x_j}\right]+P_k-\beta_k\rho k\omega+P_{kb} \tag{A.4}$$

$$\frac{\partial}{\partial x_j}\left(\rho u_j\omega\right)=\frac{\partial}{\partial x_j}\left[\left(\mu+\frac{\mu_t}{\sigma_{\omega1}}\right)\frac{\partial \omega}{\partial x_j}\right]+\frac{\alpha_1}{\nu_t}P_k-\beta_1\rho k\omega^2+P_{\omega b} \tag{A.5}$$

where σ_{k1}, β_k, $\sigma_{\omega1}$, α_1 and β_1 are the model constants, $\sigma_{k1}=\sigma_{\omega1}$=2, α_1=5/9, β_k=0.09, β_1=0.075; P_{kb} and $P_{\omega b}$ are the buoyancy production term in the k-equation and ω-equation, respectively; since the SCO2 inlet temperature is low, the two production terms are ignored.

The ω-transformed standard k-ε turbulence model is given by [36]:

$$\frac{\partial}{\partial x_j}\left(\rho u_j k\right)=\frac{\partial}{\partial x_j}\left[\left(\mu+\frac{\mu_t}{\sigma_{k2}}\right)\frac{\partial k}{\partial x_j}\right]+P_k-\beta_k\rho k\omega+P_{kb} \tag{A.6}$$

$$\frac{\partial}{\partial x_j}\left(\rho u_j\omega\right)=\frac{\partial}{\partial x_j}\left[\left(\mu+\frac{\mu_t}{\sigma_{\omega2}}\right)\frac{\partial \omega}{\partial x_j}\right]+\frac{\alpha_2}{\nu_t}P_k-\beta_2\rho k\omega^2+\frac{2\rho}{\sigma_{\omega2}\omega}\frac{\partial k}{\partial x_j}\frac{\partial \omega}{\partial x_j}+P_{\omega b} \tag{A.7}$$

where σ_{k2}, $\sigma_{\omega2}$, α_2 and β_2 are the model constants, σ_{k2}=1, $\sigma_{\omega2}$=1/0.856, α_2=0.44, β_2=0.0828.

The shear stress transport (SST) k-ω turbulence model was employed here. The model is generated by blending the Wilcox k-ω turbulence model expressed by Eqs. (A.4) and (A.5) and the standard k-ε turbulence model given by Eqs. (A.6) and (A.7) and written as [36].

$$\frac{\partial}{\partial x_j}\left(\rho u_j k\right)=\frac{\partial}{\partial x_j}\left[\left(\mu+\frac{\mu_t}{\sigma_{k3}}\right)\frac{\partial k}{\partial x_j}\right]+P_k-\beta_k\rho k\omega+P_{kb} \tag{A.8}$$

$$\frac{\partial}{\partial x_j}\left(\rho u_j\omega\right)=\frac{\partial}{\partial x_j}\left[\left(\mu+\frac{\mu_t}{\sigma_{\omega3}}\right)\frac{\partial \omega}{\partial x_j}\right]+\frac{\alpha_3}{\nu_t}P_k-\beta_3\rho k\omega^2+(1-F_1)\frac{2\rho}{\sigma_{\omega2}\omega}\frac{\partial k}{\partial x_j}\frac{\partial \omega}{\partial x_j}+P_{\omega b} \tag{A.9}$$

where σ_{k3}, $\sigma_{\omega3}$, α_3 and β_3 are the blended model constants, σ_{k3}=$F_1\sigma_{k1}$+β_1(1-F_1)σ_{k2}, $\sigma_{\omega3}$= $F_1\sigma_{\omega1}$+(1-F_1) $\sigma_{\omega2}$, α_3=$F_1\alpha_1$+(1-F_1) α_2, and β_3=$F_1\beta_1$+(1-F_1) β_2; F_1 is the blending function, F_1=1 at wall, F_1=0 in core flow, and 0<F_1<1 between wall and core flow. A specific expression for F_1 is written as [36,45]:

$$\begin{cases} F_1=\tanh\left(\xi_1^4\right) \\ \xi_1=\min\left(\max\left(\frac{\sqrt{k}}{\beta_k\omega y_n},\frac{500\nu}{y_n^2\omega}\right),\frac{4\rho k}{\xi_2\sigma_{\omega2}y_n^2}\right) \\ \xi_2=\max\left(\frac{2\rho}{\sigma_{\omega2}\omega}\frac{\partial k}{\partial x_j}\frac{\partial \omega}{\partial x_j},1.0\times10^{-10}\right) \end{cases} \tag{A.10}$$

where ν is the kinematic viscosity of SCO2, y_n is the distance to the nearest wall. The SST is handled by limiting the eddy viscosity in the following model [45]:

$$\begin{cases} \mu_t=\min\left(\frac{\rho k}{\omega},\frac{a_1\rho k}{\gamma F_2}\right),\gamma=\sqrt{2\gamma_{ij}\gamma_{ij}},\gamma_{ij}=\frac{1}{2}\left(\frac{\partial u_i}{\partial x_j}+\frac{\partial u_j}{\partial x_i}\right) \\ F_2=\tanh\left(\xi_3^2\right),\xi_3=\max\left(\frac{2\sqrt{k}}{\beta_k\omega y_n},\frac{500\nu}{y_n^2\omega}\right) \end{cases} \tag{A.11}$$

where a_1 is a constant, a_1=0.31, γ is the magnitude of the strain rate, γ_{ij} is the strain rate tensor.

In the SST model, a blended wall function, i.e., Automatic Near-Wall Treatment in ANSYS CFX, was employed to model the viscous sublayer. The blended wall function is a function of y^+(=$u_\tau y_n/\nu$), where u_τ is the friction velocity of SCO2 at wall, $u_\tau=\sqrt{\tau_w/\rho}$. In the blended wall function, ω and u_τ at y_n are calculated by the solutions of the viscous sub-layer and logarithmic law layer [45]:

$$\begin{cases} \omega_n=\sqrt{\omega_{vis}^2+\omega_{log}^2},\omega_{vis}=\frac{6\nu}{\beta_1 y_n^2},\omega_{log}=\frac{u_\tau}{a_1\kappa y_n} \\ u_\tau=4\sqrt{\left(u_\tau^{vis}\right)^4+\left(u_\tau^{log}\right)^4},u_\tau^{vis}=\frac{u_n}{y^+},u_\tau^{log}=\frac{u_n}{\frac{1}{\kappa}\ln(y^+)+5.2} \end{cases} \tag{A.12}$$

where ω_{vis} and ω_{log} are the ω values calculated by the solutions of the viscous sub-layer and logarithmic law layer, ω_n is the ω value at y_n, u_τ^{vis} and u_τ^{log} are the friction velocities at wall by using the wall shear stresses which are estimated with the solutions of the viscous sub-layer and logarithmic law layer, u_n is the fluid velocity at y_n.

In the blended wall function of ANSYS CFX, the following empirical correlation is used to determine the dimensionless temperature in convective heat transfer [45,46]:

$$\begin{cases} T^+ = Pry^+e^{-\Gamma} + [0.1\ln(y^+) + \beta]e^{-1/\Gamma}, \Gamma = \dfrac{0.01(Pry^+)^4}{1 + 5Pr^3y^+} \\ q_w = \dfrac{\rho c_p u_\tau}{T^+}(T_w - T_n), Pr = \dfrac{\mu c_p}{\lambda}, \beta = \left(3.85Pr^{1/3} - 1.3\right) + 0.1\ln(Pr) \end{cases} \tag{A.13}$$

where T^+ is the dimensionless temperature in the boundary layer, Γ is the auxiliary variable for T^+, q_w is the wall heat flux, c_p is the specific heat capacity of SCO2 at constant pressure, T_w is the wall temperature, T_n is the SCO2 temperature at y_n, β is the auxiliary variable for T^+, Pr is the SCO2 Prandtl number.

A2. Validation

The experimental mean heat transfer coefficient h_0 of the inner tube in the counter-flow tube-in-tube heat exchanger in [27] at various SCO2 inlet temperatures was used to validate the flow and heat transfer models and numerical methods in ANSYS CFX. As done in [29], the heat exchanger is simplified to a sole tube model, as shown in Fig. A1(a), where the annulus between the inner tube and the outer tube is deleted, and the water-cooling effect on the hot SCO2 is represented with a known experimental uniform outwards wall heat flux q_w. Since the tube model is geometrically symmetric and in horizontal orientation, only half of the tube was simulated to consider buoyancy effect, or the tube can be simplified to two-dimensional fluid domain.

The CFD software ANSYS CFX 2019 R2 was applied to perform SCO2 forced convective heat transfer simulations in the sole tube model. The flow and heat transfer models and wall function are described by Eqs. (A.1)–(A.9), respectively. Both temperature- and pressure-dependent SCO2 thermophysical and transport property constants were calculated by using the REFPROP Version 9.0 program [28], and a real gas property table file was generated based on them and read into CFX-Pre to interpolate these constants with local temperature and pressure in the fluid domain.

The governing equations, Eqs. (A.1)–(A.9), were discretised in the fluid domain by using finite volume method and the co-located pressure-velocity coupling equation was established between Eqs.(A1) and (A2). The complete discretisation process was present concisely in [36]. The high-resolution scheme was selected for the advection terms on the left-hand side of Eqs. (A.2)–(A.9) in the Solver Control Panel of CFX-Pre. The root-mean-square tolerance residual error of variables in those equations was specified to be 10^{-4} in the panel.
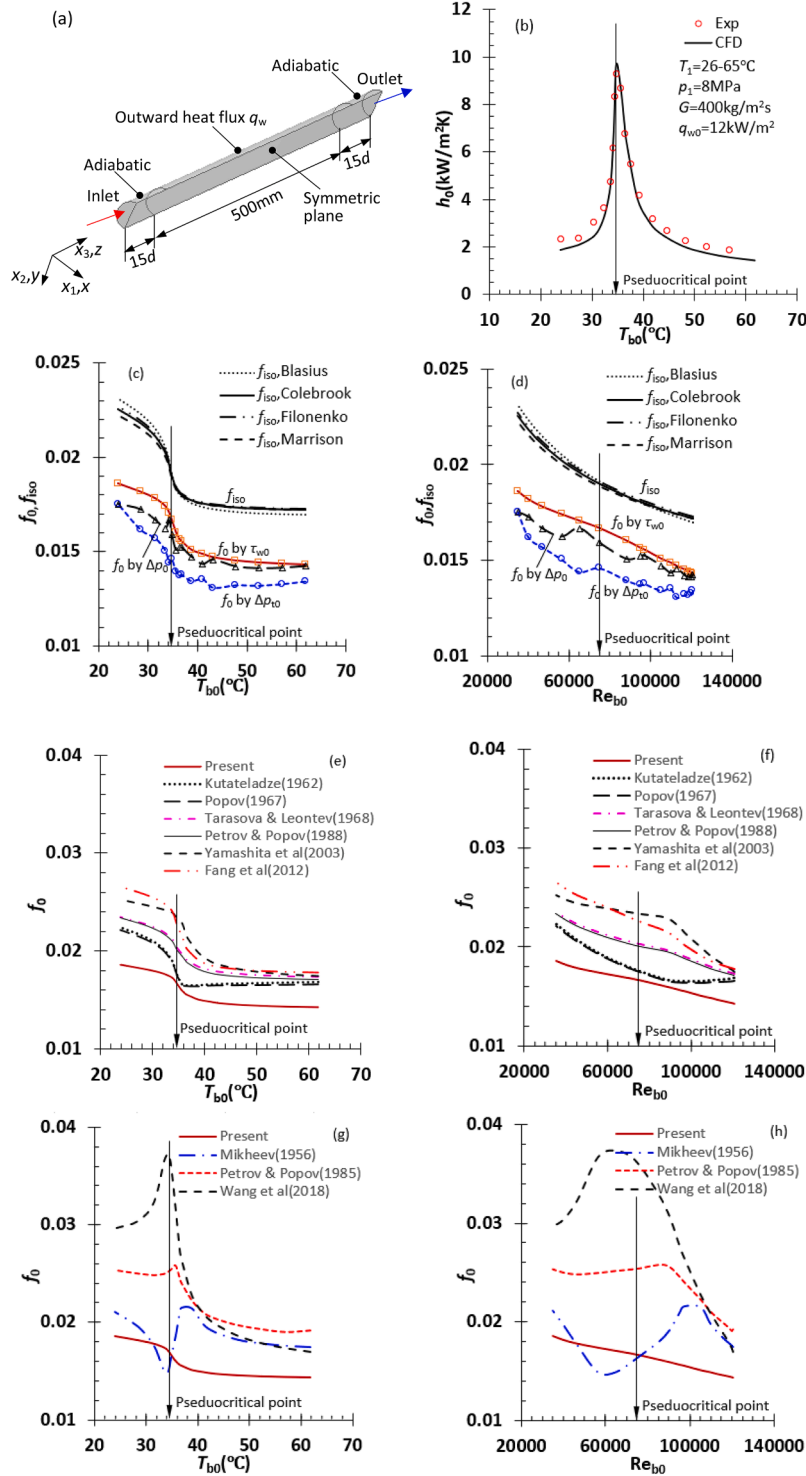
Fig. A1. Sole tube model of the water-cooled SCO2 counter-flow tube-in-tube heat exchanger in [27] and comparison of mean heat transfer coefficient h_0 between experiment and CFD simulation as well as comparison of isothermal friction factor f_{iso} and thermal friction factor f_0 between CFD simulations and predictions made by four empirical formulas in the literature, (a) geometrical model, (b) mean heat transfer coefficient h_0 versus SCO2 bulk temperature T_{b0}, (c) f_{iso} versus T_{b0}, (d) f_{iso} versus SCO2 bulk Reynolds number Re_{b0}, (e) and (g) f_0 versus T_{b0}, (f) and (h) f_0 versus Re_{b0}, the experimental data from [27].

A known SCO2 pressure p_1 and temperature T_1, zero velocity gradient and 5 % turbulence intensity are given at the tube inlet, and a SCO2 mass flow rate $\dot{m}$ is prescribed at the tube outlet. A known uniform outwards wall heat flux q_w is assigned to the tube wall, the walls of two extension tubes are subject to zero wall heat flux (adiabatic). All the walls are smooth, and no slip condition is imposed on them.

A set of wedge element dominant mesh (2524,343 elements) with an inflation layer near the walls was generated, and the corresponding y^+ values are ranged in 1.01–3.50, depending on inlet temperature. The values of boundary conditions and mesh information are tabulated in Table A1.

Table A1

Boundary conditions and mesh information for validation of flow and heat transfer models and numerical methods.

Type	Item		Value
Boundary condition	$T_1(°C)$		65, 60, 55, 50, 45, 42.5, 40, 37.5, 37, 36, 35, 34.5, 34, 32.5, 30, 26
	$G(\text{kg/m}^2\,\text{s})$		400
	$d(\text{mm})$		6
	$\dot{m}(\text{kg/s})$		$\pi G d^2/4$
	$p_1(\text{MPa})$		8
	$q_w(\text{kW/m}^2)$		12
Mesh information	Element size(mm)		0.375
	Nodes		1039,065
	Elements	Total	2524,343
		Tet4	883,103(35 %)
		Wed6	1641,240(65 %)
	Element quality		0.3518±0.3583
	Aspect ratio		24.04±27.27
	Skewness		0.1462±0.1178
	Orthogonal quality		0.8524±0.1171
	Inflation boundary layer	First layer height (mm)	0.004
		Number of layers	15
		Growth rate	1.2
		y^+	1.01, 1.14, 1.30, 1.54, 1.77, 2.05, 2.42, 2.65, 2.72, 2.98, 3.13, 3.23, 3.35, 3.43, 3.47, 3.50

where Tet4–4-node tetrahedral element, Wed6–6-node wedge element, d–inner diameter of the tube, mm, $\dot{m}$–mass flow rate of SCO2, kg/s, y^+–dimensionless wall distance, $y^+ = y_n u_\tau /\nu$, y_n–distance of a mesh node to the nearest wall, u_τ – friction velocity of SCO2 at the nearest wall, ν–kinematic viscosity of SCO2.

The predicted mean heat transfer coefficient h_0 is validated by the experimental data in [27], but the estimated Darcy friction factor f_0 has to be compared with the f_0 values predicted by using a few popular empirical formulas for smooth pipes/tubes in the literature due to the lack of experimental data on f_0 in [27]. The mean heat transfer coefficient h_0 is calculated by:

$$h_0 = \frac{q_w}{T_{b0} - T_{w0}} \tag{A.14}$$

where q_{w0} is the given wall heat flux over the plain tube, T_{b0} is SCO2 bulk temperature in the plain tube, and it is the arithmetic mean of the area-averaged SCO2 temperatures in the inlet and outlet of the tube and ten cross-sections uniformly distributed as in [27] in the tube; T_{w0} is the area-averaged wall temperature of the plain tube. The mean friction factor f_0 in the plain tube is calculated in three ways, i.e., mean wall shear stress τ_{w0} [30], static pressure drop Δp_0 [30] and total pressure drop Δp_{t0}:

$$f_0 = \frac{8\tau_{w0}}{\rho_{b0} u_{b0}^2}, \; f_0 = \frac{\Delta p_0}{\rho_{b0}\frac{L}{d}\frac{u_{b0}^2}{2}}, \; f_0 = \frac{\Delta p_{t0}}{\rho_{b0}\frac{L}{d}\frac{u_{b0}^2}{2}} \tag{A.15}$$

where τ_{w0} is area-averaged wall shear stress, ρ_{b0} and u_{b0} are SCO2 bulk density and velocity in the plain tube, which are the arithmetic means of the area-averaged SCO2 densities and velocities in the inlet and outlet and ten cross-sections in the tube, respectively; L is the plain tube length, L=500 mm, d is the plain tube inner diameter, d=6 mm, Δp_0 and Δp_{t0} are the SCO2 static pressured drop and total pressure drop across the tube, respectively.

SCO2 mean heat transfer coefficient h_0 inside the plain tube wall and non-isothermal Darcy friction factor f_0 across the tube were calculated based on the CFD simulation results and are plotted in Fig. A1(b)-(d) against the SCO2 bulk temperature T_{b0} or bulk Reynolds number Re_{b0}, where $Re_{b0}=\rho_{b0} u_{b0}/\mu_{b0}$, ρ_{b0} and μ_{b0} are SCO2 bulk density and dynamic viscosity in the tube, respectively. The mean error of the heat transfer coefficient between simulation and experiment is -5.7 ± 8.8 %. This fact suggests that the heat transfer coefficient is underestimated by 5.7 % on average with CFD simulation.

The popular empirical formulas of the isothermal and non-isothermal Darcy friction factors f_{iso}, f_0 for smooth tubes are listed in Table A2. Based on Fig. A1(c) and (d) the difference in f_{iso} values predicted by the four empirical formulas is very marginal. However, the predicted f_0 values by using CFD simulation are much smaller than those estimated isothermal friction factor f_{iso} with the empirical formulas. For example, the f_0 values calculated from the area-averaged wall shear stress τ_{w0} given by CFD simulation are $(-15.5\sim-14.7)$ % smaller than the values predicted with these empirical formulas, depending on specific formula. The f_0 values predicted by using CFD simulation based on Δp_0 and Δp_{t0} not only exhibit even large errors compared with those estimated with the empirical formulas but also are remarkably noisy against the bulk temperature and Reynolds number. Therefore, they are discarded in the paper.

Table A2

Popular empirical formulas of isothermal and non-isothermal Darcy friction factors f_{iso}, f_0 for smooth tubes or pipes.

Thermal condition	Contributor	Empirical formula	Re_{b0} range	Fluid	Source
Isothermal	Blasius (1911)	$f_{iso} = 0.3164/Re_{b0}^{-0.25}$	[4 × 10³,10⁵]	Newtonian fluid	[30]
	Colebrook (1936)	$f_{iso} = [1.8\log_{10}(Re_{b0}/7)]^{-2}$	[5 × 10³,10⁸]		[47]
	Filonenko (1954)	$f_{iso} = [1.82\log_{10}Re_{b0} - 1.64]^{-2}$	[3 × 10³,10⁶]		[48]

(continued on next page)

Table A2 (*continued*)

Thermal condition	Contributor	Empirical formula	Re_{b0} range	Fluid	Source
	Morrison (2013)	$f_{iso} = \dfrac{64}{Re_{b0}} + \dfrac{0.0304\left(\frac{3170}{Re_{b0}}\right)^{0.165}}{1 + \left(\frac{3170}{Re_{b0}}\right)^{7.0}}$	$[10^2, 10^7]$		[49]
Non-isothermal	Kutateladz (1962)	$f_0 = f_{iso}\left(\dfrac{2}{\sqrt{T_{w0}/T_{b0}}+1}\right)^2$, where $f_{iso} = [1.82\log_{10}Re_{b0} - 1.64]^{-2}$	Smooth regime	Unclear	[1]
	Popov (1967)	$f_0 = f_{iso}\left(\dfrac{\rho_{f0}}{\rho_{b0}}\right)^{0.74}$, where ρ_{f0} is fluid density at temperature $T_{f0} = (T_{w0} + T_{b0})/2$, here $\rho_{f0} \approx (\rho_{w0} + \rho_{b0})/2$, $f_{iso} = [1.82\log_{10}Re_{b0} - 1.64]^{-2}$	Smooth regime	CO2	[1]
	Tarasova & Leontev (1968)	$f_0 = f_{iso}\left(\dfrac{\mu_{w0}}{\mu_{b0}}\right)^{0.22}$, where μ_{w0} is fluid dynamic viscosity at wall, μ_{b0} is bulk temperature, $f_{iso} = [1.82\log_{10}Re_{b0} - 1.64]^{-2}$	Smooth regime	Unclear	[1]
	Petrov & Popov (1988)	$f_0 = f_{iso}\left(\dfrac{\mu_{w0}}{\mu_{b0}}\right)^{1/4} + 0.17\left(\dfrac{\rho_{w0}}{\rho_{b0}}\right)^{1/3}f_{a0}$, where f_{a0} is friction factor due to fluid acceleration, $f_{a0} = -\dfrac{8q_{w0}}{G}\left(\dfrac{\beta_v}{c_p}\right)_{b0}$, β_v is fluid thermal expansion coefficient, $f_{iso} = [1.82\log_{10}Re_{b0} - 1.64]^{-2}$	Smooth regime	water, helium & CO2	[1,50]
	Yamashita et al. (2003)	$f_0 = f_{iso}\left(\dfrac{\mu_{w0}}{\mu_{b0}}\right)^{0.72}$, where $f_{iso} = \dfrac{0.314}{0.7 - 1.65\log_{10}Re_{b0+}(\log_{10}Re_{b0})^2}$	Smooth regime	R22	[51]
	Fang et al. (2012)	$f_0 = f_{iso}\left(\dfrac{\mu_{w0}}{\mu_{b0}}\right)^{0.49\left(\frac{\rho_{f0}}{\rho_{cr}}\right)^{1.31}}$, where $f_{iso} = 1.613\left\{ln\left[0.234\left(\frac{\epsilon}{d}\right)^{1.1007} - \dfrac{60.525}{Re_{b0}^{1.1105}} + \dfrac{56.291}{Re_{b0}^{1.0712}}\right]\right\}^{-2}$, where ϵ is wall roughness, ϵ=0.5 µm in [1]	$[3 \times 10^3, 10^8]$	R410A, R404A, CO2 & R22	[1]
	Mikheev (1956)	$f_0 = f_{iso}\left(\dfrac{Pr_{w0}}{Pr_{b0}}\right)^{1/3}$, where Pr_{w0} is Prandtl number of fluid at wall, Pr_{b0} is Prandtl number of fluid at bulk temperature, $f_{iso} = [1.82\log_{10}Re_{b0} - 1.64]^{-2}$	Smooth regime	Water	[1]
	Petrov & Popov (1985)	$f_0 = f_{iso}\dfrac{\rho_{w0}}{\rho_{b0}}\left(\dfrac{\mu_{w0}}{\mu_{b0}}\right)^{0.023\left(\frac{q_{w0}}{G}\right)^{0.42}}$, where $f_{iso} = [1.82\log_{10}Re_{b0} - 1.64]^{-2}$	$[3.1 \times 10^4, 8 \times 10^5]$	CO2	[1,50]
	Wang et al. (2018)	$f_0 = 0.95 f_{iso}Pr_{b0}^{0.26}\left(\dfrac{\rho_{w0}}{\rho_{b0}}\right)^{-0.35}\left(\dfrac{\mu_{w0}}{\mu_{b0}}\right)^{0.56}$, where $f_{iso} = [1.82\log_{10}Re_{b0} - 1.64]^{-2}$	Smooth regime	Water	[52]

Based on Fig. A1(e)-(h), the predicted f_0 values by using CFD simulation are basically below the non-isothermal friction factors estimated by nine empirical formulas in Table A2 except the formula of Mikheev (1956). Additionally, the f_0 values estimated by the various empirical formulas exhibit a great variation at given bulk temperature or Reynolds number in comparison with each other except the formulas of Kutateladz (1962) and Popov (1967). The predicted f_0 values by using CFD simulation are so close to the friction factors determined by the correlations of Kutateladz (1962) and Popov (1967) that the mean error is as small as -10.7 %.

Under heating conditions, the SCO2 acceleration along the tube plays an important role in its determination of friction factor [53]. The acceleration effect on friction factor has been considered in the empirical formulas of Petrov & Popov (1988). In order to estimate the non-isothermal friction factor by utilizing the empirical correlation, the SCO2 $(\beta_v/c_p)_{b0}$ is expressed as a function of bulk temperature at p_1=8 MPa based on the REFPROP Version 9.0 program. The expression is written as:

$$\left(\dfrac{\beta_v}{c_p}\right)_b = \begin{cases} 1.7240 \times 10^{-9}T_{b0}^3 - 1.5255 \times 10^{-6}T_{b0}^2 + 4.5001 \times 10^{-4}T_{b0} - 4.4250 \times 10^{-2}, & T_{b0} \le 308K \\ -4.5845 \times 10^{-11}T_{b0}^3 + 4.6438 \times 10^{-8}T_{b0}^2 - 1.5736 \times 10^{-5}T_{b0} + 1.7894 \times 10^{-3}, & T_{b0} > 308K \end{cases} \tag{A16}$$

According to (A16), the mean percentage of f_{a0} in f_0 is -9.41 %, while the percentage of the term $0.17(\rho_{w0}/\rho_{b0})^{1/3}f_{a0}$ owing to SCO2 deceleration in f_0 is -1.70 % only under cooling conditions in the paper. Thus, the effect of SCO2 deceleration in the tube on non-isothermal friction factor can be ignored here.

In Fig. A1(g) and (h), the f_0 values estimated by the correlation of Mikheev (1956) show a dramatic reduction around the pseudocritical point. To uncover the reason behind this effect, SCO2 Prandtl number Pr_{b0}, specific heat capacity c_{pb0}, dynamic viscosity μ_{b0} and thermal conductivity λ_{b0} at bulk temperature T_{b0} along with the counter-part namely Pr_{w0}, c_{pw0}, μ_{w0} and λ_{w0} at wall temperature T_{w0} are illustrated in Fig. A2 in terms of T_{b0}. It is shown that the peak Pr_{b0} occurs at the pseudocritical point, but the peak Pr_{w0} emerges at a temperature slightly higher than the critical temperature. The mismatch of the peak positions of Pr_{b0} and Pr_{w0} should be responsible for the variation pattern of the f_0 values estimated by the correlation of Mikheev (1956). The Pr_{b0} and Pr_{w0} variation pattern is relevant to the c_{pb0} and c_{pw0} curves in Fig. A2(b) because of $Pr_{b0} = c_{pb0}\mu_{b0}/\lambda_{b0}$ and $Pr_{w0} = c_{pw0}\mu_{w0}/\lambda_{w0}$.
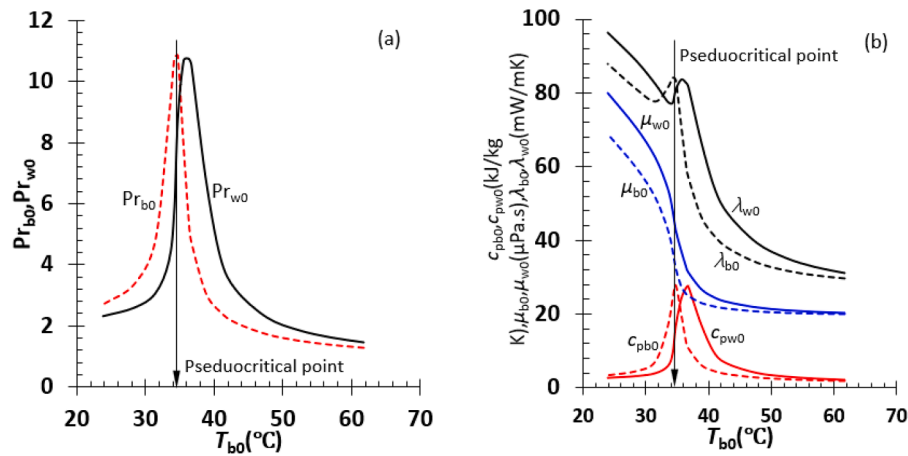
Fig. A2. SCO2 Prandtl number Pr_{b0}, specific heat capacity c_{pb0}, dynamic viscosity μ_{pb0} and thermal conductivity λ_{b0} at bulk temperature T_{b0} and the counter-part such as Pr_{w0}, c_{pw0}, μ_{w0} and λ_{w0} at wall temperature T_{w0} are plotted as a function of T_{b0} at p_1=8 MPa, T_1=26–65 °C, G=400 kg/m²s,and q_{w0}=12kWW/m², (a) Prandtl number, (b) specific heat capacity, dynamic viscosity and thermal conductivity.

Furthermore, the f_0 values predicted by the correlations of Petrov & Popov(1985) and Wang et al.(2018) demonstrate a peak near the pseudoc-ritical point and level off on both the sides of the point. This variation tendency disagrees the CFD simulation results. Therefore, these empirical formulas are not suitable for the SCO2, particularly, the correlation of Wang et al.(2018) is for water in supercritical condition. The more f_0 correlations for supercritical water were reviewed in [54] and no longer repeated here.

References

[1] X. Fang, Y. Xu, X. Su, R. Shi, Pressure drop and friction factor correlations of supercritical flow, Nucl. Eng. Des. 242 (2012) 323–330.

[2] W. Li, Z. Yu, Heat exchangers for cooling supercritical carbon dioxide and heat transfer enhancement: a review and assessment, Energy Rep. 7 (2021) 4085–4105.

[3] N.S. Sohoni, V.M. Kriplani, Review of heat transfer enhancement techniques in swirl flow using active and passive methods, Int. J. Eng. Res. Technol. 6 (1) (2013) 86–94.

[4] M. Jadhav, R. Awari, D. Bibe, A. Bramhane, M. Mokashi, Review on enhancement of heat transfer by active method, Int. J. Curr. Eng. Technol. (2016) 221–225. Vols. special issue-6.

[5] K. Kuwahara, S. Higashiiue, D. Ito and, et al., Experimental study on cooling heat transfer of supercritical carbon dioxide inside horizontal micro-fin tubes, Trans. JSRAE 24 (3) (2007) 173–181.

[6] H.S. Lee, H.J. Kim, J.I. Yoon, K.H. Choi, C.H. Son, The cooling heat transfer characteristics of the supercritical CO_2 in micro-fin tube, Heat Mass Transf. 49 (2) (2013) 173–184.

[7] Y. Li, F. Sun, G. Xie, B. Sunden, J. Qin, Numerical investigation on flow and thermal performance of supercritical CO_2 in horizontal cylindrically concaved tubes, Appl. Therm. Eng. 153 (2019) 655–668.

[8] L. Chai, S.A. Tassou, Effect of cross-section geometry on the thermohydraulic characteristics of supercritical CO_2 in minichannels, Energy Procedia 161 (2019) 446–453.

[9] M. Yang, G. Li, F. Liao, J. Li, X. Zhou, Numerical study of characteristic influence on heat transfer of supercritical CO_2 in helically coiled tube with non-circular cross section, Int. J. Heat Mass Transf. 176 (2021), 121511.

[10] B. Pei, Z. Chen, F. Li, B. Bai, Flow and heat transfer of supercritical CO_2 in the honeycomb ultra-compact plate heat exchanger, J. Supercrit. Fluids 148 (2019) 1–8.

[11] Z. Wang, G. Li, Y. Zhang, F. Wang, X. Jiang, Z. Ma, Flow and heat transfer investigation of supercritical carbon dioxide in a novel biomimetic honeycomb fractal gas cooler of transcritical CO_2 heat pumps, Therm. Sci. Eng. Prog. 37 (2023) 101533.

[12] J. Zhao, L. Li, W. Xie, H. Zhao, Flow and heat transfer characteristics of liquid metal and supercritical CO_2 in a twisted tube heat exchanger, Int. J. Therm. Sci. 174 (2022), 107453.

[13] M. Hashemian, S. Jafarmadar, J. Nasiri, H.S. Dizaj, Enhancement of heat transfer rate with structural modification of double pipe heat exchanger by changing cylindrical form of tubes into conical form, Appl. Therm. Eng. 118 (2017) 408–417.

[14] J. Hao, C. Ju, C. Li, L. Tian, Z. Ge, X. Du, Comparison and evaluation of supercritical CO_2 cooling performance in horizontal tubes with variable cross-section by field synergy theory, Int. J. Energy Res. 46 (2022) 14133–14144.

[15] Z. Yi, Y. Xu, X. Chen, Cooling heat transfer of supercritical CO_2 in diverging and converging microtubes, Chem. Eng. Technol. 45 (2) (2022) 302–308.

[16] T. Cong, B. Wang, H. Gu, Numerical analysis on heat transfer enhancement of sCO2 in the tube with twisted tape, Nucl. Eng. Des. 397 (2022), 111940.

[17] W. Li, Z. Yu, Y. Wang, Y. Li, Heat transfer enhancement of twisted tape inserts in supercritical carbon dioxide flow conditions based on CFD and vortex kinematics, Therm. Sci. Eng. Prog. 31 (2022), 101285.

[18] H. Meng, Y. Yao, Y. Yu, B. Shi, P. Ding, Enhancement analysis of turbulent flow and heat transfer of supercritical CO_2 in a static mixer with three helical blades, Korean J. Chem. Eng. 40 (1) (2023) 79–90.

[19] W. Li, G. Yu, Z. Yu, Bioinspired heat exchangers based on triply periodic minimal surfaces for supercritical CO_2 cycles, Appl. Therm. Eng. 179 (2020), 115686.

[20] W. Li, W. Li, Z. Yu, Heat transfer enhancement of water-cooled triply periodic minimal surface heat exchangers, Appl. Therm. Eng. 217 (2022), 119198.

[21] W.T. Ji, J.F. Fan, C.Y. Zhao, W.Q. Tao, A revised performance evaluation method for energy saving effectiveness of heat transfer enhancement techniques, Int. J. Heat Mass Transf. 138 (2019) 1142–1153.

[22] L. Ma, W. Liu, Z.C. Liu, J.G. Yang, J. Yang, S.Y. Wang, K. Yang, A.W. Fan and X.M. Huang, "Heat transfer pipe". China Patent CN102564189A, 11 07 2012.

[23] J. Yang, L. Ma, J. Liu, W. Liu, Thermal–hydraulic performance of a novel shell-and-tube oil cooler with multi-fields synergy analysis, Int. J. Heat Mass Transf. 77 (2014) 928–939.

[24] Z.M.A. Alsulaiei, H.M. Hasan, M.H. Fagr, Flow and heat transfer in obstacled twisted tubes, Case Stud. Therm. Eng. 7 (2021), 101286.

[25] A.K.A. Razzaq, K.S. Mushatet, A numerical study for a double twisted tube heat exchanger, Int. J. Heat Technol. 39 (5) (2021) 1583–1589.

[26] A.K.A. Razzaq, K.S. Mushatet, Evaluation the performance of the double tube heat exchanger by using combined twisted tube and nano fluid, Int. J. Mech. Eng. 7 (1) (2022) 6618–6628.

[27] C. Dang, E. Hihara, In-tube cooling heat transfer of supercritical carbon dioxide, Part 1 Experimental measurement, Int. J. Refrig. 27 (2004) 736–747.

[28] E.W. Lemmon, M.O. McLinden, M.L. Huber, REFPROP Documentation, Release 10.0, National Institute of Standards and Technology, Gaithersburg, USA, 2018.

[29] W. Li, Z. Yu, Y. Wang, Y. Li, Heat transfer of supercritical carbon dioxide in a tube-in-tube heat exchanger-a CFD study, J. Supercrit. Fluids 181 (2022), 105493.

[30] F.M. White, Fluid Mechanics, 7th ed., McGraw-Hill Companies, Inc., New York, 2011.

[31] ANSYS, ANSYS CFX Reference Guide, ANSYS, Inc., Southpointe, USA, 2013.

[32] S.M. Liao, T.S. Zhao, An experimental investigation of convection heat transfer to supercritical carbon dioxide in miniature tubes, Int. J. Heat Mass Transf. 45 (2002) 5025–5034.

[33] Z. Du, W. Lin, A. Gu, Numerical investigation of cooling heat transfer to supercritical CO_2 in a horizontal circular tube, J. Supercrit. Fluids 55 (2010) 116–121.

[34] J. Wang, Z. Guan, H. Gurgenci, K. Hooman, A. Veeraragavan, X. Kang, Computational investigations of heat transfer to supercritical CO_2 in a large horizontal tube, Energy Convers. Manage. 157 (2018) 536–548.

[35] J. Wang, Z. Guan, H. Gurgenci, A. Veeraragavan, X. Kang, Y. Sun, K. Hooman, Numerical study on cooling heat transfer of turbulent supercritical CO_2 in large horizontal tubes, Int. J. Heat Mass Transf. 126 (2018) 1002–1019.

[36] ANSYS, ANSYS CFX-Solver Theory Guide, ANSYS, Inc., Canonsburg, 2011.

[37] S. Yang, L. Zhang, H. Xu, Experimental study on convective heat transfer and flow resistance characteristics of water flow in twisted elliptical tubes, Appl. Therm. Eng. 31 (2011) 2981–2991.

[38] M. Talebi, F. Lalgani, Assessment of thermal behavior of variable step twist in the elliptical spiral tube heat exchanger, Int. J. Therm. Sci. 170 (2021), 107126.

[39] P.M. Ligrani, M.M. Oliveira, T. Blaskovich, Comparison of heat transfer augmentation techniques, AIAA J. 41 (3) (2003) 337–362.

[40] L. Wang, Y.C. Pan, J.D. Lee, Y. Wang, B.R. Fu, C. Pan, Experimental investigation in the local heat transfer of supercritical carbon dioxide in the uniformly heated horizontal miniature tubes, Int. J. Heat Mass Transf. 159 (2020), 120136.

[41] L. Wang, Y.C. Pan, J.D. Lee, Y. Wang, B.R. Fu, C. Pan, Convective heat transfer characteristics of supercritical carbon dioxide in vertical miniature tubes of a uniform heating experimental system, Int. J. Heat Mass Transf. 167 (2021), 120833.

[42] Z.Y. Guo, D.Y. Li, B.X. Wang, A novel concept for convective heat transfer enhancement, Int. J. Heat Mass Transf. 41 (14) (1998) 2221–2225.

[43] F. Kock, H. Herwig, Local entropy production in turbulent shear flows: a high-Reynolds number model with wall functions, Int. J. Heat Mass Transf. 47 (2004) 2205–2215.

[44] S. Khanmohammadi, N. Mazaheri, Second law analysis and multi-criteria optimization of turbulent heat transfer in a tube with inserted single and double twisted tape, Int. J. Therm. Sci. 145 (2019), 105998.

[45] F. Menter, J.C. Ferreira, T. Esch and, et al., The SST turbulence model with improved wall treatment for heat transfer predictions in gas turbines, in: Proceedings of the International Gas Turbine Congress, Tokyo, 2003.

[46] B.A. Kader, Temperature and concentration profiles in fully turbulent boundary layers, Int. J. Heat Mass Transf. 24 (9) (1981) 1541–1544.

[47] C.F. Colebrook, Turbulent flow in pipes, with particular reference to the transition region between the smooth and rough pipe laws, J. Inst. Civ. Eng. 11 (4) (1939) 133–156.

[48] V. Gnielinski, Neue Gleichungen für den Wärme- und den Stoffübergang in turbulent durchströmten Rohren und Kanälen, Forsch. Ingenieurwes. 41 (1) (1975) 8–16.

[49] F.A. Morrison, An Introduction to Fluid Mechanics, Cambridge University Press, Cambridge, 2013.

[50] L. Cheng, G. Ribatski, J.R. Thome, Analysis of supercritical CO_2 cooling in macro- and micro-channels, Int. J. Refrig. 31 (2008) 1301–1316.

[51] T. Yamashita, H. Mori, S. Yoshida, M. Ohno, Heat transfer and pressure drop of a supercritical pressure fluid flowing in a tube of small diameter, Mem. Fac. Eng. 63 (4) (2003) 227–244. , Kyushu University.

[52] H. Wang, Q. Bi, G. Wu, Z. Yang, Experimental investigation on pressure drop of supercritical water in an annular channel, J. Supercrit. Fluids 131 (2018) 47–57.

[53] L. Wang, Y.C. Pan, J.D. Lee, Y. Wang, B.R. Fu, C. Pan, Experimental investigation in the pressure drop characteristics of supercritical carbon dioxide in the uniformly heated horizontal miniature tubes, J. Supercrit. Fluids 162 (2020), 104839.

[54] V.I. Deev, V. Kharitonov, A.M. Baisov, A.N. Churkin, Hydraulic resistance of supercritical pressure water flowing in channels-A survey of literature, Nucl. Eng. Des. 330 (2021), 111313.